وزارة التعليم العالي والبحث العلمي

Ministry of Higher Education and Scientific Research

BADJI MOKHTAR-ANNABA UNIVERSITY
UNIVERSITE BADJI MOKHTAR ANNABA

جامعة باجي مختار ـ عنابة ـ

Faculty of Sciences
Department of Mathematics

Year: 2025/2026

THESIS

Presented with a view to obtaining the doctorate degree

Partial Differential and Stochastic Equations in Image Processing: Applications to Medical Images

Stream
Applied Mathematics

Speciality
Differential Equations and Applications

By
HALILOU Radhia

SUPERVISOR: NOURI Fatma Zohra **Prof.** **U.B.M.- Annaba**

In front of the jury

PRESIDENT: TAALLAH Frekh	**Prof.**	**U.B.M.- Annaba**
EXAMINER: KHADIR Mohamed Tarek	**Prof.**	**U.B.M.- Annaba**
EXAMINER: MAOUNI Messaoud	**Prof.**	**UNIV.-Skikda**

وزارة التعليم العالي والبحث العلمي

Ministère de l'Enseignement Supérieur et de la Recherche Scientifique

BADJI MOKHTAR-ANNABA

UNIVERSITY

UNIVERSITE BADJI MOKHTAR

ANNABA

جامعة باجي مختار

-عنابة-

Faculté des Sciences

Département de Mathématiques

Année : 2025/2026

THÈSE

Présentée en vue de l'obtention du diplôme de Doctorat

Equations aux Dérivées Partielles et Stochastiques en Traitement d'Image: Applications aux Images Médicales

Filière
Mathématiques Appliquées

Spécialité
Équations Différentielles et Applications

Par
HALILOU Radhia

DIRECTEUR DE THÈSE: NOURI Fatma Zohra **Prof. U.B.M. – Annaba**

Devant le jury

PRESIDENT: TAALLAH Frekh	**Prof.**	**U.B.M.- Annaba**
EXAMINATEUR: KHADIR Mohamed Tarek	**Prof.**	**U.B.M.- Annaba**
EXAMINATEUR: MAOUNI Messaoud	**Prof.**	**UNIV.- Skikda**

Acknowledgements

First of all, I am grateful to **Allah**, the Almighty and Wise, who gave me the capacity, persistence, and reasoning abilities to complete the work of my thesis. I want to convey my heartfelt appreciation to my supervisor, **Professor Fatma Zohra Nouri**, for proposing a very interesting and ambitious research topic, for her invaluable advice, guidance, and unwavering encouragement throughout this research. I am very grateful for her continued help. My thanks also to **Professor Mohammed Lakhdar Hadji**, who helped me by providing valuable references related to my thesis work. I extend my thanks to the members of my thesis committee: **Professor Frekh Taallah**, for having agreed to chair the defense jury. Professors **Mohamed Tarek Khadir** and **Messaoud Maouni**, for agreeing to be examiners and taking the time to read and evaluate this work.

At last, not the least, I want to thank my family, especially **my parents**, for their continuous encouragement and moral support. I would also like to express my deepest gratitude to my **beloved husband** for his patience, understanding, and unwavering encouragement throughout this journey. His support has been an invaluable source of strength and motivation.

To my beloved children, **Hidaya** and **Abdallah**, I ask for your forgiveness for the sacrifices that this doctoral journey has required. Your patience, understanding, and love have been my greatest source of motivation.

Finally, I wish to thank all **my friends** and colleagues who accompanied me during this adventure, shared their knowledge, and offered friendship and support both inside and outside the laboratory. Their presence made this experience truly enriching and memorable.

المعادلات التفاضلية الجزئية والعشوائية في معالجة الصور: التطبيق على الصور الطبية

ملخص

تُكرّس هذه الأطروحة لدراسة وتطبيق المعادلات التفاضلية العشوائية (م.ت.ع) والمعادلات التفاضلية الجزئية العشوائية (م.ت.ج.ع) في مجال إزالة الضوضاء من الصور. تم تصميم النماذج الرياضية المقترحة بهدف تقليل الضوضاء الموجودة في الصور المتدهورة مع الحفاظ في الوقت نفسه على البُنى الأساسية والهامة في الصورة. تتضمن هذه النماذج حدود الانجراف والانتشار، المستوحاة من مناهج كلاسيكية وحديثة، بما في ذلك نموذج بيرونا-ماليك، وانجراف من نوع باربو، والانتشار وفق صيغة بوركوفسكي.

تم إجراء تحليل رياضي صارم لإثبات وجود وحيدة الحلول لكل نموذج من النماذج. وبالنسبة للنماذج القائمة على م.ت.ع يستند هذا التحليل إلى إطار حسابات Øksendal العشوائية. أما بالنسبة ل م.ت.ج.ع، فتم ضمان الصياغة الصحيحة للمشكلة من خلال شروط وفرضيات مناسبة، وفقًا للأعمال النظرية التي قام بها بن سوسان (Bensoussan).

من الناحية العددية، تم تقريب نماذج م.ت.ع باستخدام خوارزمية أويلر–مارويا ما بالتكامل مع محاكاة مونت كارلو، بينما تم حل نماذج م.ت.ج.ع باستخدام طرق الفروق المحدودة لضمان الاستقرار والدقة العددية. وقد تم تقييم فعالية النماذج على صور رمادية وملونة ثنائية الأبعاد تحتوي على ضوضاء. أظهرت التقييمات الكمية، التي أُجريت باستخدام مؤشرات جودة قياسية مثل نسبة الذروة للإشارة إلى الضوضاء (PSNR) و مؤشر التشابه الهيكلي (SSIM)، قدرة النماذج العشوائية على استعادة جودة الصور بشكل فعّال. وتؤكد النتائج أن إدخال مكون عشوائي في عملية إزالة الضوضاء يوفر إطارًا قويًا ومرنًا لاستعادة الصور.

الكلمات المفتاحية: المعادلات التفاضلية العشوائية، المعادلات التفاضلية الجزئية العشوائية، إستعادة الصور، تقليل الضوضاء.

Partial Differential and Stochastic Equations in Image Processing: Application to Medical Images

Abstract

This thesis is devoted to the study and application of stochastic differential equations (SDEs) and stochastic partial differential equations (SPDEs) for image denoising. The proposed mathematical models are designed to reduce noise in corrupted images while preserving essential structural features. These models incorporate drift and diffusion terms inspired by both classical and contemporary approaches, notably the Perona-Malik model, Barbu-type drift, and Borkowski's diffusion formulation. A rigorous mathematical analysis is conducted to establish the existence and uniqueness of weak solutions for each model. In the case of SDEs, this analysis is based on the framework of stochastic calculus developed by Øksendal. For SPDEs, the well-posedness of the problem is ensured by imposing appropriate conditions and hypotheses, following the theoretical contributions of Bensoussan. From a numerical perspective, the SDE-based models are discretized using the Euler–Maruyama scheme combined with Monte Carlo simulations, while SPDEs are solved using finite difference methods to ensure both stability and accuracy. The performance of the proposed models is evaluated on both grayscale and color images contaminated with noise. Quantitative assessments using standard image quality metrics such as Peak Signal-to-Noise Ratio (PSNR) and Structural Similarity Index Measure (SSIM) demonstrate the effectiveness of the stochastic models in restoring image quality. The results confirm that introducing stochasticity into the denoising process offers a robust and flexible framework for image restoration.

Keywords: Stochastic Differential Equations (SDEs), Stochastic Partial Differential Equations (SPDEs), Denoising and Restoring Images .

Equations aux dérivées partielles et Stochastique en Traitement d'image: Application aux images Médicales

Résumé

Cette thèse est consacrée à l'étude et à l'application des équations différentielles stochastiques (EDS) et des équations aux dérivées partielles stochastiques (EDPS) dans le domaine du débruitage d'images. Les modèles mathématiques proposés sont conçus pour réduire le bruit présent dans les images dégradées tout en préservant leurs structures essentielles. Ces modèles intègrent des termes de dérive et de diffusion inspirés à la fois d'approches classiques et modernes, notamment le modèle de Perona-Malik, la dérive de type Barbu, et la diffusion selon la formulation de Borkowski. Une analyse mathématique rigoureuse est menée afin d'établir l'existence et l'unicité des solutions faibles pour chaque modèle. Pour les modèles basés sur les EDS, cette analyse repose sur le cadre du calcul stochastique développé par Øksendal. Concernant les EDPS, la bonne formulation du problème est garantie en imposant des conditions et hypothèses appropriées, suivant les travaux théoriques de Bensoussan.

D'un point de vue numérique, les modèles à base d'EDS sont discrétisés à l'aide du schéma d'Euler–Maruyama combiné à des simulations de Monte Carlo, tandis que les EDPS sont résolues à l'aide de méthodes de différences finies afin d'assurer stabilité et précision. L'efficacité des modèles est évaluée sur des images en niveaux de gris et couleur bruitées.

Les évaluations quantitatives, effectuées à l'aide d'indicateurs standards de qualité d'image tels que le PSNR (Peak Signal-to-Noise Ratio) et le SSIM (Structural Similarity Index Measure), démontrent la capacité des modèles stochastiques à restaurer efficacement la qualité des images. Les résultats confirment que l'introduction d'une composante stochastique dans le processus de débruitage constitue un cadre robuste et flexible pour la restauration d'images.
Mots-clés: Equations Différentielle Stochastique, Equations Différentielle Partielle Stochastique, Débruitage et restauration des images.

Contents

List of Figures

Introduction

In practical applications, digital images are often corrupted by noise during the acquisition process leading to degradation. This degradation can result from a wide range of factors, including sensor limitations, environmental conditions (such as low light or motion), thermal noise, electronic interference, and transmission errors. Such imperfections are particularly common in applications involving low-cost sensors, rapid image capture, or long-distance signal transmission. The presence of noise can significantly degrade the visual quality and interpretability of images. Denoising image data plays a critical role in enhancing image quality, especially its structure.

To address this issue, image denoising techniques have become an essential component of image processing. These techniques aim to suppress or eliminate noise while preserving important features such as edges, textures, and structural details. The effectiveness of a denoising algorithm is typically measured by its ability to improve image clarity without introducing artifacts or blurring significant content.

This can be applied across numerous domains; For example, in medical imaging, it enhances diagnostic accuracy by clarifying anatomical structures in MRI, CT, and ultrasound scans. In remote sensing and satellite imagery, it improves the readability of data and environmental monitoring results. While in video surveillance, it contributes to better object detection and scene interpretation under low-light or adverse conditions. Furthermore, in fields such as astronomy, microscopy, and autonomous navigation, denoising is indispensable

for extracting meaningful information from noisy visual data. As such, the development of robust and efficient denoising algorithms remains a central challenge in the field of image analysis.

The earliest mathematical methods were inspired by physical diffusion processes. Back in 1984, Koenderink [49] introduced the idea of using the heat equation to smooth images, where the approach involves convolving the image with a Gaussian kernel, simulating a uniform spread of information. While this method reduces noise effectively, it also tends to blur important features, especially edges.

To overcome this inconvenience, Perona-Malik (PM) [63] proposed a major improvement in 1990 with their anisotropic diffusion model. Their idea was to adapt the amount of smoothing based on local intensity changes encouraging diffusion in flat regions while preserving edges. This was a turning point, as it brought nonlinear partial differential equations (PDEs) into image processing field.

Later on variational methods gained popularity, notably the total variation (TV) model introduced by P. Getreuer [37]. This approach balances staying close to the original noisy image with regularization that favors sharp edges. It is well known for its ability to reduce noise without sacrificing important structures.

Over time, a range of other techniques emerged:

- Spectral methods, like Fourier Analysis[68], [72] and [74]; and wavelets transform techniques [29] and [33], which enable multi-scale analysis of images;
- Non-local methods, such as the Non-Local Means filter [19], which take advantage of repeating patterns in the image by comparing similar patches, even if they're far apart;
- Statistical approaches, including Bayesian models [45], Markov Random Fields [34], and Maximum A Posteriori (MAP) estimation [8].

Recently, a new research in image processing based on stochastic differential equations (SDEs)

[4], [5], [15], [16], [17], [26] and [27], has been developed taking the advantage of the fact that there is a relationship between the SDEs and PDEs (see for example [24], [31], [69] and [79]), leading to better results. The relationship between SDEs and PDEs is a probabilistic approach of a PDE that allows expressing their solutions in the form of the expectation of a certain function of a stochastic process. Furthermore, according to Itô and Kolmogorov formula [61] and [42], we can move from one to another.

In this work, we first highlight two types of SDEs to image enhancement, one was introduced by Barbu et al [5], where the authors set the diffusion to 1 and the other by Borkowski et al [15] who neglected the drift term. Based on these two SDEs, we propose a model, combining drift and diffusion terms from Barbu and Borkowski SDEs together with PM functions [63]. We start by showing the well-posedness of the derived models, then we proceed to their discretizations by Euler-Maruyama method.

The second mathematical technique used to solve the noisy image problem is based on stochastic partial differential equations (SPDEs). The evolution of SPDEs in image denoising reflects a broader trend in applying stochastic methods to image processing tasks. By integrating randomness into the modeling process, SPDE-based approaches offer enhanced flexibility and robustness, resulting in more effective noise reduction and better preservation of essential image features.

In this part, we focus on the restoration of noisy images and propose a novel SPDE that extends the Perona–Malik (PM) framework [63] by incorporating a stochastic component. This modification allows the proposed model to more effectively capture the stochastic nature of noise. While the original PM model is known for its effectiveness, it suffers from ill-posedness, which limits its practical applicability. To address this issue, we adopt the regularization technique introduced by Catté et al. in 1992 [20], which replaces the gradient term $|\nabla u|$ with its smoothed estimate $|\nabla G_\sigma * u|$. This adjustment ensures the model's consistency and well-posedness. We conduct a mathematical analysis of the proposed SPDE

by using the deterministic framework of Catté et al. and the theory of weak solutions developed by Bensoussan and Temam (1971) [10]. To approximate the solution, we employ a finite difference method and analyze its stability using Fourier analysis techniques. Numerical experiments confirm the effectiveness of the proposed models in improving image quality while preserving fine details, demonstrating substantial improvements in noise reduction and feature preservation.

The work of this thesis presents a detailed study of several approaches related to image processing, and is organized as follows:

Chapter 1 introduces the fundamental concepts of digital and numerical images, image degradation models, and image restoration techniques. We present the basic definitions and notations necessary for a clear understanding of the work, and we emphasize the role of mathematical modeling in image processing. In particular, we recall classical restoration models and illustrate their behavior in order to highlight their strengths and limitations.

In Chapter 2; we introduce the mathematical background required throughout our work. We start with a presentation of basic mathematical concepts, followed by a discussion of functional spaces including Banach and Hilbert spaces, which are crucial for analyzing existence and uniqueness results. The chapter then we describe the stochastic framework, establishing the probabilistic tools needed to study stochastic differential and partial differential equations.

Chapter 3 highlight the usefulness of stochastic differential equations (SDEs) in image restoration as well as their main properties. We present several related works in the field of image denoising using SDEs, outlining their advantages and limitations. Our contribution is introduced through the formulation of a family of SDE's models, where the drift and diffusion terms are carefully chosen to capture the image anisotropic behavior. In particular, we investigate five different cases corresponding to distinct choices of drift and diffusion functions, each motivated by classical PDE-based models such as PM, Barbu's drift, and Borkowski's

diffusion. The proposed equations are solved numerically using the Euler–Maruyama scheme, and its stability analysis is provided to ensure the reliability of the method. Finally, numerical results are presented on both grayscale and color images, and the performance of the different SDE models is compared with the obtained results by some existing SDE and PDE-based techniques. The evaluation relies on standard image quality measures, including the Peak Signal-to-Noise Ratio (PSNR) and the Structural Similarity Index (SSIM), which confirm the effectiveness of the proposed approach.

In Chapter 4, we extend the stochastic framework to stochastic partial differential equations (SPDEs) for image restoration. More precisely, we consider a stochastic variant of the Perona–Malik model, where the deterministic PDE is perturbed by a Wiener process to better capture noise and uncertainty in images. We begin with a rigorous mathematical study of the proposed SPDE, focusing on the existence and uniqueness of weak solutions. This analysis is carried out using a stochastic process defined in a separable Hilbert space H, which provides a solid framework for ensuring the well-posedness of the model. A stability analysis is then conducted to ensure the reliability of the discretization using finite difference schemes. Finally, numerical results are presented on grayscale images, demonstrating the model's ability to reduce noise while preserving edges and main structures. In the same way as in chapter 3, we evaluate the standard image measures (PSNR and SSIM) performance of our proposed models.

Chapter 1

Principles of image representation

1.1 Introduction

This chapter begins by presenting fundamental definitions and essential image information, including the notion of a digital image, image formats, color representations, main image categories, and key characteristics used to describe image content. We then discuss noise and image degradation, introducing the principal noise types and their effects on image quality. The chapter proceeds with an overview of image restoration and its main tasks, focusing in particular on denoising and deblurring. Basic mathematical tools required for these operations such as the gradient, Laplacian, divergence, and convolution operators are then summarized. Finally, we review classical PDE-based approaches for image restoration, distinguishing between isotropic diffusion models and anisotropic diffusion techniques, which play a central role in modern edge-preserving restoration methods.

1.2 Fundamental definitions

Definition 1.1. (Signal) A signal is a physical quantity that varies over time, used to convey either energy or information. Generally, two types are distinguished:

- **Power signals:** which carry energy (e.g., electrical signals).
- **Information signals:** which transmit information (e.g., images, videos, sound).

Definition 1.2. (Pixel/Voxel) In image representation, the smallest unit of information is referred to as a pixel in two-dimensional (2D) images and a voxel in three-dimensional (3D) images. A pixel corresponds to a point on a discrete 2D grid, while a voxel extends this notion to 3D, representing a small cube within a volume. Both pixels and voxels are characterized by their spatial position within the image domain and an associated numerical value, often called intensity, which encodes information such as brightness, color, or other attributes.

Definition 1.3. (Image) An image is defined as a two-dimensional **signal** that assigns an intensity or a set of intensities to each point of a spatial domain. Formally, an image is represented as a function

$$I : \Omega \subset \mathbb{R}^2 \to \mathbb{R}^m,$$

where Ω denotes the spatial domain and m is the number of channels.

- For $m = 1$, the image is grayscale and $I(x, y)$ represents the intensity at position (x, y).
- For $m = 3$, the image is a color image composed of several components such as RGB channels.

1.3 Digital image

A digital image is an approximation of a real-world scene (a three-dimensional reality) obtained using image capture devices, called digitizers, such as digital cameras or scanners. The conversion from an analog signal to a digital one is performed in two steps:

Sampling: periodically extracting samples from a continuous signal.

Quantization: assigning a numerical value to each sampled point (for further details on

these procedures, see [2, 48]).

A digital image is therefore represented in a two- or three-dimensional discrete domain and defined by pixel or voxel elements. These elements are arranged on a regular grid, where each pixel/voxel is characterized by its spatial position X and an associated numerical value $f(X)$, referred to as its **intensity**. Specifically, $X = (x, y)$ in the 2D case and $X = (x, y, z)$ in the 3D case. Accordingly, images are stored in computers using a discrete representation. For mathematical analysis, it is generally assumed that the discretization is sufficiently fine so that these discrete signals can be approximated by continuous (or at least piecewise continuous) functions (see [35]).

A continuous representation of a digital image is defined over a closed domain $\mathbb{R}^d$, where $d = 2$ for 2D images and $d = 3$ for 3D images. Thus, a digital image results from discretizing both the spatial coordinates and the intensity values of a continuous image. It can be viewed as a finite matrix (or tensor in the 3D case) of values, each corresponding to a pixel or voxel in the image (Figure 1.1).

For a 2D image:

$$f = f(x_i, y_j), \quad 0 \leq i \leq M,\ 0 \leq j \leq N, \tag{1.1}$$

For a 3D image:

$$f = f(x_i, y_j, z_k), \quad 0 \leq i \leq M,\ 0 \leq j \leq N,\ 0 \leq k \leq H, \tag{1.2}$$

where $f(x_i, y_j)$ denotes the intensity of the pixel at row i and column j in 2D, while $f(x_i, y_j, z_k)$ denotes the intensity of the voxel at position (i, j, k) in 3D. Here, M, N, and H represent the dimensions of the image.

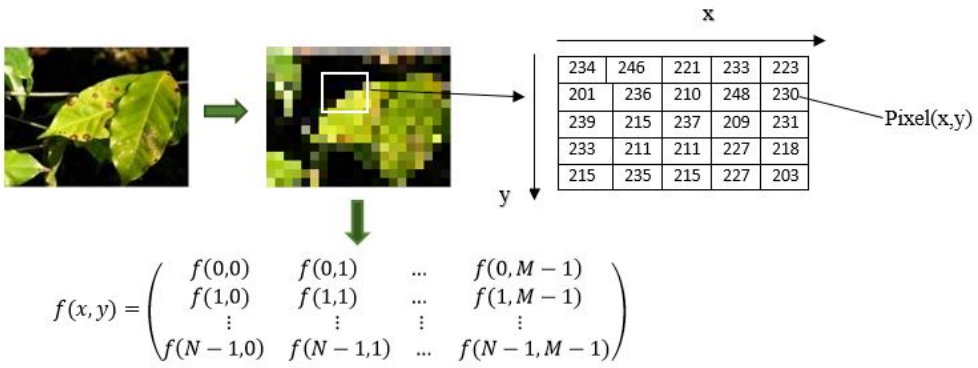

Figure 1.1: Illustration of a digital image as a matrix of pixels.

Color modes

The definition of an image can also be expressed in terms of its color representation. Several color modes are commonly used, including:

Mode	Definition	Pixel values	Bits	Colors
Bitmap	Black/White	0 or 1	1 bit	2
Grayscale	Gray levels	0–255	8 bits	256
RGB	Red, Green, Blue	0–255 each	24 bits	$256^3 = 16,777,216$
CMYK	Cyan, Magenta, Yellow, Black	0–255 each	32 bits	$256^4 = 4,294,967,296$

Table 1.1: Color modes in digital images

Image formats

An image format summarizes the properties of an image (e.g., file size, quality), which may vary significantly from one format to another. Some examples are presented below:

Format	Type	Modes Supported	Compression
GIF	Matrix	Binary, Grayscale, RGB	Lossless
TIFF	Matrix	All modes	Lossless
JPEG	Matrix	Grayscale, RGB, CMYK	Lossy
EPS	Vector	All modes	Depends
PGM	Matrix	Grayscale	Lossless

Table 1.2: Common image formats

Data compression: It consists in reducing the file size. Depending on the compression method used, the image quality may be significantly reduced. Two main techniques are distinguished:

- **Lossless compression**: reduces file size without loss of detail or color.
- **Lossy compression**: ignores some image information, which reduces its quality.

Characteristics of an image

An image is characterized by the following features:

- **Image size**: it is total number of pixels.
- **Resolution**: number of pixels per inch (1 inch = 2.54 cm).
- **File size (weight)**: it is known by total number of bytes (1 byte = 8 bits).
- **Color coding**: as the value stored in each pixel to represent its color.

Using this coding, images are classified according to their colors, which is referred to the color mode.

Categories of image

We distinguish two broad categories of images:

1. **Matrix image**: In image processing, a matrix image (also called a raster image) is a digital image represented by a two-dimensional grid of pixels, where each pixel contains intensity or color information. The image is stored as a matrix (2D array), with each entry corresponding to a pixel value.

   - Advantages: it is capable of representing highly detailed and continuous-tone images such as photographs.

   - Disadvantages: it loses quality when enlarged, since the fixed number of pixels becomes apparent, resulting in pixelation or blurring.

   - Examples: JPEG, PNG, GIF, BMP.

   - Applications: Digital photography, scanned images, web graphics, and digital painting.

2. **Vector image**: A vector image is a digital image defined using mathematical formulas that describe geometric primitives such as points, lines, curves, and shapes. Unlike raster images, vector images do not store individual pixel values but rather instructions for reconstructing the image.

   - Advantages: it can be scaled to any resolution without quality loss, making them resolution-independent.

   - Disadvantages: it not suitable for complex, detailed, or photographic content, as representing such variations mathematically is inefficient.

   - Examples: SVG, EPS, AI.

   - Applications: Logos, icons, illustrations, fonts, and graphics that require frequent resizing.

1.3.1 Noise and image degradation

Image degradation refers to the deterioration of image quality caused by factors such as noise, blur, or distortions during acquisition, transmission, or storage. It alters the original information and motivates the need for restoration techniques.

Definition 1.4 (Noise)**.** A noise is a random parasitic phenomenon caused by various sources (light, acquisition devices, motion, etc.).

Types of noise

1. **Additive noise**: A noise is said to be additive when an initial image I_0 is combined with a noise component G to produce a noisy image I, as expressed by the following formula.

$$I(i,j) = I_0(i,j) + G(i,j),$$

where G is a random variable with mean 0.

Example (Additive white Gaussian noise): Gaussian noise is obtained by adding to each pixel a random value that follows a Gaussian probability distribution

$$G(x,y) = \frac{1}{2\pi\sigma^2} e^{-\frac{(x-\mu_x)^2+(y-\mu_y)^2}{2\sigma^2}},$$

where σ is the variance and μ is the mean.

2. **Multiplicative noise**: A noise is said to be multiplicative if we take an initial image I_0 and multiply it by a noise G in order to obtain a noisy image I, which is represented by the following formula:

$$I(i,j) = I_0(i,j) \cdot G(i,j),$$

where G has mean 1.

Example: Speckle noise, i.e:

$$I_{\text{speckle}}(x) = I(x)\,(1 + \eta(x)),$$

where $\eta(x)$ is a zero-mean noise process.

3. **Convolutional noise**: Noise is said to be convolutive if we take an initial image I_0 and convolve it with a noise G in order to obtain a noisy image I, which is represented by the following formula:

$$I(i,j) = I_0(i,j) * G(i,j)$$

where G is a random variable with mean equal to 1.

Example: Motion blur.

Criteria for denoising evaluation

Digital images are subject to a wide variety of degradations during acquisition, processing, compression, storage, and transmission, which can result in a loss of visual quality. The method of assessing image quality based on human judgment relies on the analysis of certain criteria such as the dynamic range of the image, the relationship between definition (size) and resolution, geometric distortions, and the presence of noise. However, this subjective evaluation is generally impractical, time-consuming, and costy.

In order to automatically predict image quality, so-called objective evaluation methods have been developed, which are based on explicit quantitative measures. These methods are also widely used to assess and optimize image processing systems and algorithms. This is done by comparing a reference image (the original image) with a test image (the post-processed image). In this context, the simplest and most widely used quality measure is the Mean

Squared Error (MSE), computed from:

$$MSE(u_0, u) = \frac{1}{M.N} \sum_{i=1}^{M} \sum_{j=1}^{N} \left(u_0(i,j) - u(i,j)\right)^2 \tag{1.1.1}$$

where u_0 denotes the original image and u the processed image, both of size $M \times N$.

Another measure directly derived from the MSE is the Peak Signal-to-Noise Ratio (PSNR), given by:

$$PSNR(u_0, u) = 10 \log_{10}\left(\frac{L^2}{MSE(u_0, u)}\right) \tag{1.1.2}$$

where L corresponds to the maximum possible intensity value in the image ($L = 255$ for a grayscale image).

Instead of using error accumulation methods (like in (1.1.1)), Wang *et al.* [74] developed the Structural Similarity Index Measure (SSIM), defined as:

$$SSIM = \left[l(u_0, u)\right]^{\alpha} \cdot \left[c(u_0, u)\right]^{\beta} \cdot \left[s(u_0, u)\right]^{\gamma} \tag{1.1.3}$$

with

$$\begin{cases} l(u_0, u) = \dfrac{2\mu_{u_0}\mu_u + c_1}{\mu_{u_0}^2 + \mu_u^2 + c_1} \\ c(u_0, u) = \dfrac{2\sigma_{u_0}\sigma_u + c_2}{\sigma_{u_0}^2 + \sigma_u^2 + c_2} \\ s(u_0, u) = \dfrac{\sigma_{u_0} + c_3}{\sigma_{u_0}^2 + \sigma_u^2 + c_3} \end{cases}$$

The first term $l(u_0, u)$ of (1.1.3) is the **luminance comparison function**, which measures the closeness of the mean luminance values (μ_{u_0} and μ_u) of the two images. This factor reaches its maximum value of 1 only when $\mu_{u_0} = \mu_u$.

The second term $c(u_0, u)$ is the **contrast comparison function**, which measures the similarity of contrast between the two images. Here, contrast is measured by the standard deviations σ_{u_0} and σ_u. This term also reaches its maximum value of 1 only when $\sigma_{u_0} = \sigma_u$.
The third term $s(u_0, u)$ is the **structure comparison function**, which measures the correlation coefficient between the two images u_0 and u, where $\sigma_{u_0 u}$ denotes their covariance. The positive constants c_1, c_2, and c_3 are introduced to avoid division by zero, while the three parameters α, β, and γ define the relative importance of each term.
It should be noted that the SSIM takes values in the interval $[0, 1]$, where a value of 0 means there is no similarity between the two images u_0 and u, while a value of 1 indicates that they are identical.
There exist many other image quality measures discussed in [3, 30]. However, to this day, there is no universal quality measure, since each one has its own sensitivity to specific types of degradation. For example, some studies [73, 41, 3] have shown that MSE, and therefore PSNR, unlike SSIM, perform poorly when evaluating geometric distortions, because different types of degradations applied to the same image can yield the same MSE value. On the other hand, the same studies have shown that MSE, and consequently PSNR, are more effective when assessing the quality of noisy images.
Since there are no precise rules for choosing between SSIM or PSNR in image quality evaluation, in our numerical experiments we estimate **both values**.

1.3.2 Image restoration

Image restoration techniques seek to counteract the effects of degradation and reconstruct an image that approximates its original or intended form as closely as possible. This process typically involves analyzing the degraded image and applying mathematical algorithms or filtering methods to suppress or eliminate noise, blur, and other distortions. The overarching objectives are to enhance visual quality, improve interpretability, and facilitate the accurate

extraction of meaningful information from the image.

Several restoration tasks exist, depending on the type of degradation:

- **Denoising**: aims to reduce unwanted random noise while preserving important structures such as edges and textures. Methods include linear and nonlinear filters, variational models, PDE-based approaches, and modern stochastic or deep-learning strategies.

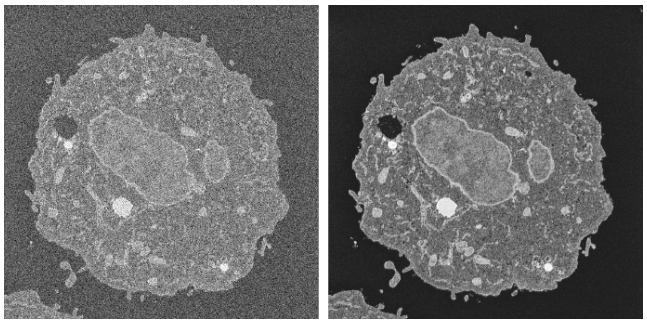

Figure 1.2: Illustration of noise removing

- **Deblurring**: focuses on removing blur caused by motion, defocus, or atmospheric turbulence. Classical approaches include inverse filtering, Wiener filtering, and regularized optimization methods to deal with the ill-posed nature of the problem.

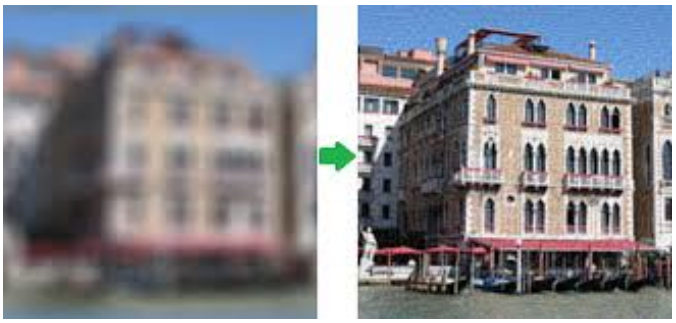

Figure 1.3: Restoration of a Blurred Image via Deblurring

- **Inpainting**: addresses the reconstruction of missing or corrupted regions of an image in a visually coherent manner. It is widely used for object removal, scratch repair, and

image completion, often relying on diffusion, variational, or patch-based models.

Figure 1.4: Example of inpainting image technique

1.3.3 Basic mathematical tools

In this part, we assume that the image $I : \mathbb{R}^d \to \mathbb{R}$ is twice continuously differentiable ($I \in C^2(\mathbb{R}^d)$). Its first- and second-order partial derivatives with respect to the spatial coordinates X are denoted as:

$$I_x = \frac{\partial I}{\partial x}, \quad I_y = \frac{\partial I}{\partial y}, \quad I_z = \frac{\partial I}{\partial z}, \quad I_{xx} = \frac{\partial^2 I}{\partial x^2}, \quad I_{xy} = \frac{\partial^2 I}{\partial x \partial y}. \tag{1.1.4}$$

The gradient of I, denoted by ∇I, is given by:

$$\nabla I = \begin{cases} (I_x, I_y)^T & \text{when } d = 2, \\ (I_x, I_y, I_z)^T & \text{when } d = 3. \end{cases} \tag{1.1.5}$$

The divergence of I, denoted by $\operatorname{div} I$, is defined as:

$$\operatorname{div} I = \begin{cases} I_x + I_y & \text{when } d = 2, \\ I_x + I_y + I_z & \text{when } d = 3, \end{cases} \tag{1.1.6}$$

The Laplacian of I, denoted by ΔI, is defined as:

$$\Delta I = \begin{cases} I_{xx} + I_{yy} & \text{when } d = 2, \\ I_{xx} + I_{yy} + I_{zz} & \text{when } d = 3. \end{cases} \tag{1.1.7}$$

The directional derivative of an image along a vector $V \in \mathbb{R}^d$, denoted I_V, is:

$$I_V = \frac{\partial I}{\partial V} = \nabla I \cdot V, \tag{1.1.8}$$

and explicitly:

$$I_V = \begin{cases} v_1 I_x + v_2 I_y & \text{for } d = 2,\ V = (v_1, v_2)^T, \\ v_1 I_x + v_2 I_y + v_3 I_z & \text{for } d = 3,\ V = (v_1, v_2, v_3)^T. \end{cases} \tag{1.1.9}$$

The second directional derivative of an image along a vector $V \in \mathbb{R}^d$, denoted I_{VV}, is:

$$I_{VV} = \frac{\partial^2 I}{\partial V^2} = \nabla\big(\nabla I \cdot V\big) \cdot V, \tag{1.1.10}$$

and explicitly:

$$I_{VV} = \begin{cases} v_1^2 I_{xx} + 2v_1 v_2 I_{xy} + v_2^2 I_{yy}, & d = 2,\ V = (v_1, v_2)^T, \\ v_1^2 I_{xx} + 2v_1 v_2 I_{xy} + v_2^2 I_{yy} + 2v_1 v_3 I_{xz} + 2v_2 v_3 I_{yz} + v_3^2 I_{zz}, & d = 3,\ V = (v_1, v_2, v_3)^T. \end{cases} \tag{1.1.11}$$

The level set of I associated with a value a is defined as:

$$\Gamma_a(I) = \{X \in \mathbb{R}^d \mid I(X) = c\}. \tag{1.1.12}$$

A contour in an image corresponds to an abrupt change in gray level (intensity) and therefore

to an accumulation of level set boundaries, called isophotes (level lines). The gradient is often used to analyze intensity variations in the image: its direction points toward the variations (when non-zero it is perpendicular to level lines and thus to contours), while its norm, denoted $\|\nabla I\|$, measures their strength and is computed as:

$$\|\nabla I\| = \begin{cases} \sqrt{I_x^2 + I_y^2} & \text{when } d = 2, \\ \sqrt{I_x^2 + I_y^2 + I_z^2} & \text{when } d = 3. \end{cases} \tag{1.1.13}$$

Thus, it is possible to define an orthonormal basis at each point of the image from the gradient and its orthogonal (see Figure 1.5), given by the vectors:

$$\xi = \frac{\nabla I}{\|\nabla I\|}, \qquad \eta = \frac{\nabla^{\perp} I}{\|\nabla I\|}, \tag{1.1.14}$$

where $\nabla^{\perp} I = (-I_y, I_x)$ denotes the orthogonal vector to ∇I.

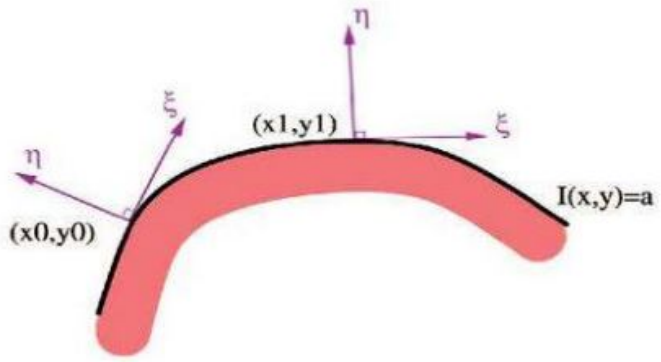

Figure 1.5: Illustration of the level set $I(x, y) = a$

1.4 PDE-Based approaches for image restoration

Partial Differential Equations (PDEs) are mathematical expressions involving an unknown function that depends on several variables. Since they describe continuous changes, PDEs are

widely used to model a broad range of physical phenomena: thermodynamics (heat equation), hydrodynamics (Navier–Stokes equations), electromagnetism (Maxwell's equations), optics (optical flow equation), among many others.

Image restoration is one of the central procedures in digital image processing. Its goal is to improve the quality of an image, either for human observers or as a preprocessing step in computer vision systems. A key challenge in this approach is to distinguish between the significant features of the image, which should be preserved, recovered, or even enhanced, and the unwanted components, regarded as noise, which must be removed.

In this section, we provide a brief overview of several classes of PDE-based image processing methods that guided our thinking in developing the restoration approaches presented in the following chapters. It should be noted that we describe only methods used for 2D images; the corresponding equations for 3D images are quite similar or can be found in the references cited in the text.

1.4.1 Isotropic diffusion

Heat Equation

Several studies [78] have proposed a multi-scale analysis of images through successive convolutions of the original image with a series of Gaussian kernels of increasing standard deviation σ. This procedure allows, among other things, the removal of image information exhibiting spatial variations at scales smaller than σ, resulting in simplified representations of the image. Such a linear process is commonly employed to reduce noise while obtaining a more reliable estimate of image structures.

Koenderink [49] demonstrated that similar results can be obtained via the following evolutionary process:

$$\frac{\partial I}{\partial t} = \Delta I, \tag{1.3}$$

with the initial condition $I(X,0) = I_0$, representing the original image to be processed (the initial conditions are the same for all methods presented in this thesis and will therefore not be explicitly repeated). The boundary conditions on the image domain boundary $\partial\Omega$ are given by:

$$\nabla I(X) \cdot n = 0, \quad \forall X \in \partial\Omega, \tag{1.4}$$

where n denotes the outward normal vector on the boundary.

Equation (1.3) corresponds to iteratively filtering the image I_0 by adding its Laplacian at each iteration. A multi-scale family $I(X,t)$ is thus obtained, where the time variable t serves as a scale parameter (for examples of multi-scale analysis applications, see [52, 53, 44, 76]). It is noteworthy that equivalent results can also be obtained by convolving the image with a Gaussian kernel whose standard deviation is $\sigma = \sqrt{2t}$.

The use of the heat PDE is motivated by considering the distribution of gray levels in the image as a uniform distribution of heat intensities. The process of information diffusion is interpreted as heat conduction in an isotropic material perfectly insulated from its environment, hence the Neumann boundary conditions (1.4). This enables diffusion in all directions in an unbiased manner (isotropic diffusion), without accounting for the image structures. Such a diffusion scheme leads to mixing of intensity values, which significantly blurs edges. Figure 1.6 illustrates an example where equation (1.3) is applied to an image, showing that the image progressively becomes more blurred as t increases.

Inverse Heat Equation for Image Restoration

In the context of image restoration using a simplistic approach, it therefore seems reasonable to apply the **inverse heat equation**, that is:

$$\frac{\partial I}{\partial t} = -\Delta I \tag{1.5}$$

This method provides acceptable results only for small values of t or when the image is not noisy, because the numerical solution of equation (1.5) is inherently unstable and highly sensitive to initial conditions. This is illustrated in Figure 1.7.

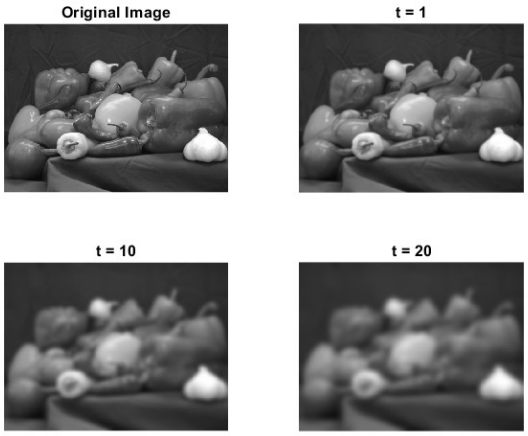

Figure 1.6: Application of the heat equation with various different times and $\Delta t = 0.1$

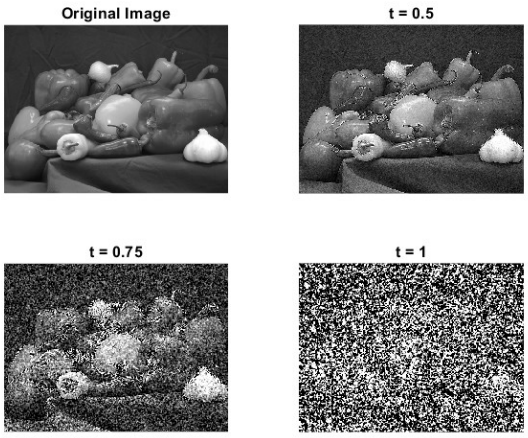

Figure 1.7: Application of the inverse heat equation at different times and $\Delta t = 0.01$

1.4.2 Anisotropic diffusion

Perona–Malik Equation

In 1987, Perona and Malik [63] introduced the concept of anisotropic diffusion. This diffusion is favored in certain directions in order to preserve edges during the diffusion process. The idea is based on the fact that Equation (1.3) can be written as:

$$\frac{\partial I}{\partial t} = \operatorname{div}(\nabla I), \tag{1.6}$$

where the authors replaced the constant conductivity of the heat equation (1.6) (i.e $c = 1$ in 1.3)with a scalar function $g(\|\nabla I\|)$ that accounts for the local properties of the image. The corresponding equation is then given by:

$$\frac{\partial I}{\partial t} = \operatorname{div}(g(\|\nabla I\|)\, \nabla I)\,. \tag{1.7}$$

Here, the function g, called the *diffusivity function* or *stopping function*, is chosen to achieve adaptive smoothing. It is defined as a decreasing function that takes large values in homogeneous regions and values close to zero in the presence of edges. Several examples of such functions can be found in [2]. In [63], the authors proposed the following functions:

$$g(\|\nabla I\|) = \frac{1}{1 + \left(\frac{\|\nabla I\|}{k}\right)^2}, \tag{1.8}$$

$$g(\|\nabla I\|) = \exp\left(-\left(\frac{\|\nabla I\|}{k}\right)^2\right), \tag{1.9}$$

where the variable k acts as a contrast parameter to distinguish between regions to be smoothed and discontinuities that must be preserved. To study the behavior of the diffusion process via Equation (1.3), some authors [22, 50] observed that, by expanding it and

using a change of basis, it can be rewritten in the following form:

$$\frac{\partial I}{\partial t} = c_\eta I_{\eta\eta} + c_\xi I_{\xi\xi}, \tag{1.10}$$

where

$$c_\eta = g(\|\nabla I\|), \qquad c_\xi = g(\|\nabla I\|) + \|\nabla I\| g'(\|\nabla I\|),$$

and $I_{\eta\eta}$ and $I_{\xi\xi}$ represent the directional derivatives along the vectors η and ξ defined in (1.1.14). Thus, the directional behavior of diffusion is easier to interpret when written in this so-called *oriented Laplacian* form.

Indeed, by plotting the curves of the functions c_η and c_ξ (see Figure 1.8), one observes that c_η and c_ξ are close to 1 in homogeneous regions, since $\|\nabla I\| \approx 0$. In this case, the local behavior of Equation (1.10) approaches that of the isotropic diffusion equation (1.3). On the other hand, as the gradient norm increases, smoothing becomes weaker in the tangential direction of the level lines because $c_\eta \to 0$, whereas in the gradient direction, one observes an *edge enhancement effect*, due to the fact that c_ξ becomes negative beyond a certain threshold depending on the parameter K

$$\|\nabla I\| > K \quad \text{for the function given in (1.8)}, \qquad \|\nabla I\| > K\sqrt{2} \quad \text{for that given in (1.9)}.$$

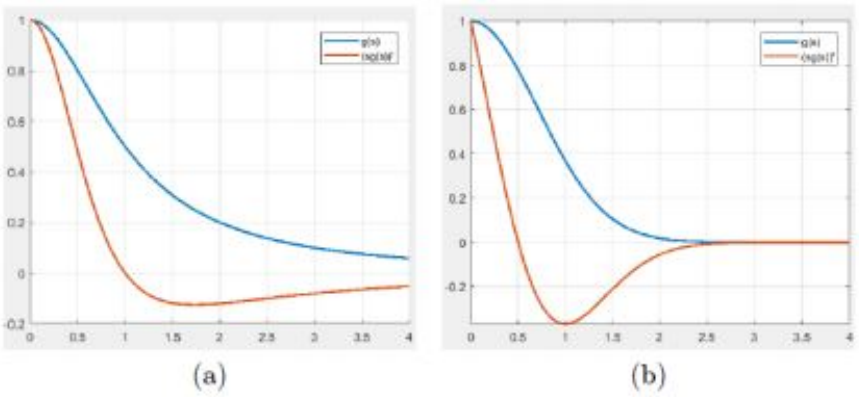

Figure 1.8: Representative curves of the coefficients c_η (in blue) and c_ξ (in orange) for (a) the rational function and (b) the exponential function.

This leads locally to a behavior similar to the *inverse heat equation* (1.5), known for its instability, in regions of very high gradient. The choice of the parameter K is generally based on prior knowledge of the image variations and is made in an adaptive way. Several studies have addressed the choice of this contrast parameter [77, 12, 51, 38], with the common point being that the choice is made globally. Other works, such as [18], determine the parameter K locally in a semi-automatic manner. More details regarding this technique will be given in the next chapter. The behavior of Equation (1.10), as described above, results in a transition between smoothing and enhancement, which significantly improves the visual appearance of the image compared to the isotropic diffusion studied in the previous section.

Nevertheless, when the image contains a high level of noise, inverse diffusion tends to amplify it instead of suppressing it. Some works have been carried out in this direction, for instance Kichenassamy [46], who showed that the Perona–Malik problem is not well-posed in the continuous framework (for a complete theoretical study, the reader may refer to [75]).

The theoretical issue raised by the previous model led to a regularized version introduced by Catté *et al.* [20]. This approach consists in pre-smoothing the image with a Gaussian kernel, which makes it possible to distinguish strong gradients due to noise from those due to structures.

This model not only overcomes the drawback of the PM model concerning noise amplification, but is also well-posed and numerically stable.

In the same framework, other researchers have proposed more complex versions (see for example [77, 59, 11]).

From these results, we can say that, Perona–Malik formulation has been the starting point for a multitude of new methods involving nonlinear PDEs in image processing.

1.5 Conclusion

In this first chapter, we introduced the fundamental principles underlying image representation and restoration. We begin with the definition of digital images and discussed the main sources of noise and degradation that affect their quality. Basic notions of image restoration were then presented, together with notations and structural aspects that will be used throughout the manuscript.

In the second part, we review PDE-based approaches for image restoration. We distinguish between isotropic diffusion, which smooths images uniformly, and anisotropic diffusion, which preserves edges and fine structures while reducing noise.

This chapter provides the essential basic concepts to be used in the next chapters of the work of this thesis. The following chapters extend these ideas to stochastic models and advanced image restoration techniques.

Chapter 2

Preliminaries and functional spaces

2.1 Introduction

In this chapter, we present the useful mathematical tools required for the development of our analytical framework. We introduce the essential functional spaces, the basic properties of norms and operators, and the notation used to represent images as functions on domains of $\mathbb{R}^2$. In addition, we recall the fundamental elements of the stochastic framework and briefly outline the numerical methods that will be employed in later chapters. The aim is to establish a precise and coherent set of preliminaries that will support both the theoretical analysis and the numerical developments presented throughout this work.

2.2 Functional spaces

Definition 2.1. A real *Banach space* V is a real vector space equipped with a norm $\|\cdot\|$, defined for every $u \in V$, and complete with respect to this norm. The norm satisfies the following properties:

- $\|u\| \geq 0$ for all $u \in V$,

- $\|u\| = 0$ if and only if $u = 0$,
- $\|\lambda u\| = |\lambda| \cdot \|u\|$ for all $\lambda \in \mathbb{R}$,
- $\|u + v\| \leq \|u\| + \|v\|$ for all $u, v \in V$.

Definition 2.2. The space V is called a *Hilbert space* when the norm is associated with an inner product:

$$\|u\| = \sqrt{(u, u)} \tag{1.1}$$

where $(u, v) \in \mathbb{R}$ is the inner product of u and v.

Properties of a real inner product:

- The inner product is bilinear,
- $(u, u) \geq 0$ for all $u \in V$,
- $(u, u) = 0$ if and only if $u = 0$,
- $(u, v) = (v, u)$ for all $u, v \in V$.

Definition 2.3. Let $\Omega \subset \mathbb{R}^n$ be an open regular set, bounded or not, and let $p \in \mathbb{R}_+$.

- For $1 \leq p < \infty$, the space $L^p(\Omega)$ consists of measurable functions such that:

$$\int_\Omega |u(x)|^p dx < \infty,$$

$$L^p(\Omega) = \{u : \Omega \to \mathbb{R} \text{ measurable } \mid \|u\|_p < \infty\}. \tag{1.2}$$

The norm in $L^p(\Omega)$ is given by:

$$\|u\|_{L^p(\Omega)} = \left(\int_\Omega |u(x)|^p dx \right)^{1/p}. \tag{1.3}$$

- For $p = \infty$, the space $L^\infty(\Omega)$ consists of measurable and bounded functions:

$$L^\infty(\Omega) = \{u : \Omega \to \mathbb{R} \text{ measurable } \mid \|u\|_\infty < \infty\}, \tag{1.4}$$

and the norm is:

$$\|u\|_{L^\infty(\Omega)} = \inf\{M \geq 0 : |u(x)| \leq M \text{ a.e. in } \Omega\}. \tag{1.5}$$

Remark 2.2.1. L^p spaces (called Lebesgue spaces) are Banach spaces.

Remark 2.2.2. When $p = 2$, the Lebesgue space is a Hilbert space.

Definition 2.4. We define the space of test functions:

$$\mathcal{D}(\Omega) = \{\varphi \in C^\infty(\Omega) \text{ such that } \operatorname{supp}(\varphi) \subset \Omega\}, \tag{1.6}$$

with:

$$\operatorname{supp}(\varphi) = \{x \in \Omega : \varphi(x) \neq 0\}. \tag{1.7}$$

Definition 2.5. A *distribution* or *generalized function* on $\Omega \subset \mathbb{R}^n$ is a linear, continuous functional L such that:

$$L : \mathcal{D}(\Omega) \to K = \mathbb{R} \text{ or } \mathbb{C}, \tag{1.8}$$

and if $\varphi_k \to 0$ in $\mathcal{D}(\Omega)$, then:

$$\lim_{k\to\infty} \langle L, \varphi_k \rangle = 0.$$

Remark 2.2.3. We write $\langle L, \varphi_k \rangle$ instead of $L(\varphi_k)$.

Definition 2.6. Let $\Omega \subset \mathbb{R}^n$, v be locally integrable on Ω, and $\beta \in \mathbb{N}^n$. We say that v is the

weak derivative of order β of a function u, denoted $D^\beta u$, if:

$$\forall \varphi \in C_c^\infty(\Omega), \quad \int_\Omega u\, \partial^\beta \varphi \, dx = (-1)^{|\beta|} \int_\Omega v\varphi \, dx. \tag{1.9}$$

Definition 2.7. Let $\Omega \subset \mathbb{R}^n$, $k \in \mathbb{N}$, and $p \in \mathbb{R}_+$. The *Sobolev space* of order k, based on L^p, denoted $W^{k,p}(\Omega)$, is the space of functions $u \in L^p(\Omega)$ whose weak derivatives of order less than or equal to k also belong to $L^p(\Omega)$:

$$W^{k,p}(\Omega) = \left\{ u \in L^p(\Omega) \mid \forall \beta,\ |\beta| \le k,\ D^\beta u \in L^p(\Omega) \right\}. \tag{1.10}$$

We equip $W^{k,p}(\Omega)$ with the norm:

$$\|u\|_{W^{k,p}(\Omega)} = \begin{cases} \left(\sum_{|\beta| \le k} \|D^\beta u\|_{L^p(\Omega)}^p \right)^{1/p}, & 1 \le p < \infty, \\ \max_{|\beta| \le k} \|D^\beta u\|_{L^\infty(\Omega)}, & p = \infty. \end{cases} \tag{1.11}$$

Remark. When $p = 2$, we denote $W^{k,2}(\Omega)$ by $H^k(\Omega)$.

Definition 2.8 (Bounded Domain)**.** A subset $D \subset \mathbb{R}^n$ is said to be a **bounded domain** if it is an open, connected set and there exists a constant $R > 0$ such that

$$D \subset B(0, R) = \{x \in \mathbb{R}^n : \|x\| < R\}.$$

In other words, D is contained in some ball of finite radius in $\mathbb{R}^n$.

Definition 2.9 (Lipschitz Boundary)**.** A domain $D \subset \mathbb{R}^n$ is said to have a **Lipschitz boundary** if, for every point $x_0 \in \partial D$, there exist:

- a neighborhood U of x_0,
- a rigid transformation of coordinates T,

- and a Lipschitz continuous function $\varphi : \mathbb{R}^{n-1} \to \mathbb{R}$,

such that, in the new coordinates,

$$T(D \cap U) = \{(x', x_n) \in \mathbb{R}^{n-1} \times \mathbb{R} : x_n > \varphi(x')\} \cap T(U),$$

and

$$T(\partial D \cap U) = \{(x', x_n) \in \mathbb{R}^{n-1} \times \mathbb{R} : x_n = \varphi(x')\} \cap T(U).$$

Definition 2.10 (Convex Domain)**.** A set $D \subset \mathbb{R}^n$ is called **convex** if for any two points $x, y \in D$, the line segment joining them is entirely contained in D; that is,

$$(1-t)x + ty \in D, \quad \forall\, t \in [0,1].$$

In particular, if D is both bounded and convex, its boundary is automatically Lipschitz continuous.

Remark 2.2.4. In image processing applications, the image domain is typically represented by a rectangular region

$$D = [0, M] \times [0, N] \subset \mathbb{R}^2 \quad \text{or} \quad D = [0, M] \times [0, N] \times [0, H] \subset \mathbb{R}^3,$$

which is both **bounded**, **convex**, and has a **Lipschitz boundary**.

2.3 Stochastic framework

In this section, we introduce the fundamental concepts required to construct and work within a stochastic framework. We start by considering a nonempty set Ω, which will serve as the sample space of our probability model.

Definition 2.11. A **σ-algebra** $\mathcal{F}$ is a collection of subsets of Ω that satisfies the following properties:

1. $\emptyset \in \mathcal{F}$ and $\Omega \in \mathcal{F}$.

2. If $A \in \mathcal{F}$, then the complement $A^c := \Omega \setminus A \in \mathcal{F}$.

3. If $A_1, A_2, \cdots \in \mathcal{F}$, then both the countable union and intersection are also in $\mathcal{F}$:

$$\bigcup_{k=1}^{\infty} A_k \in \mathcal{F}, \quad \bigcap_{k=1}^{\infty} A_k \in \mathcal{F}.$$

Definition 2.12. Let $\mathcal{F}$ be a σ-algebra over Ω. A function $P : \mathcal{F} \to [0, 1]$ is called a **probability measure** if:

1. $P(\emptyset) = 0$ and $P(\Omega) = 1$.

2. For any countable collection $A_1, A_2, \cdots \in \mathcal{F}$,

$$P\left(\bigcup_{k=1}^{\infty} A_k\right) \leq \sum_{k=1}^{\infty} P(A_k).$$

3. If the sets $A_1, A_2, \cdots \in \mathcal{F}$ are pairwise disjoint (i.e., $A_i \cap A_j = \emptyset$ for $i \neq j$), then

$$P\left(\bigcup_{k=1}^{\infty} A_k\right) = \sum_{k=1}^{\infty} P(A_k).$$

From these properties, it follows that for any $A, B \in \mathcal{F}$, if $A \subseteq B$, then $P(A) \leq P(B)$.

Definition 2.13. A **probability space** is a triple $(\Omega, \mathcal{F}, P)$, where:

- Ω is a nonempty set (called the *sample space*),

- $\mathcal{F}$ is a σ-algebra of subsets of Ω,

- P is a probability measure defined on $\mathcal{F}$.

Definition 2.14. Let $\Omega \subset \mathbb{R}^N$ be an open subset. A ***Radon measure*** μ on Ω is a linear functional defined on $C_c(\Omega)$ (the space of continuous functions with compact support in Ω), denoted by

$$\varphi \mapsto \langle \mu, \varphi \rangle,$$

such that for every compact set $K \subset \Omega$, there exists a constant $C(K) > 0$ such that

$$|\langle \mu, \varphi \rangle| \leq C(K)\|\varphi\|_\infty, \quad \text{for all } \varphi \in C_c(\Omega) \text{ with } \operatorname{supp}(\varphi) \subset K. \tag{4.2}$$

The elements of $C_c(\Omega)$ are called *test functions*.

Definition 2.15. ([1]) Let $(\Omega, \mathcal{F}, P)$ be a probability space. Then a function $X : \Omega \to \mathbb{R}$ is called a **random variable**, if the event

$$X^{-1}((-\infty, a]) \equiv \{\omega : X(\omega) \leq a\} \in \mathcal{F}$$

for each $a \in \mathbb{R}$, i.e., a random variable is a real valued $\mathcal{F}$-measurable function on $(\Omega, \mathcal{F}, P)$.

Definition 2.16. A real-valued standard Wiener process (or Brownian motion) defined on $T = \mathbb{R}_+$ or $T = [0, T]$ is a stochastic process $\{W_t; t \in T\}$ with continuous paths, satisfying the following properties:

- $W_0 = 0$ almost surely;
- For all $0 \leq s < t$, the increment $W_t - W_s$ is normally distributed with mean zero and variance $t - s$;
- For any finite sequence of times $0 = t_0 < t_1 < \cdots < t_n$, the increments $W_{t_{i+1}} - W_{t_i}$, for $0 \leq i \leq n - 1$, are independent.

Remark 2.3.1.

1. For each t, the random variable W_t is Gaussian with mean zero, i.e., $\mathbb{E}(W_t) = 0$, and variance $\mathbb{E}(W_t^2) = t$, which increases as time evolves.

2. The probability that W_t lies in a small interval $[x, x + dx]$ is given by the Gaussian density:
$$\mathbb{P}(W_t \in [x, x + dx]) = g(t, x)\, dx = \frac{1}{\sqrt{2\pi t}} \exp\left(-\frac{x^2}{2t}\right) dx.$$

2.4 Numerical methods for stochastic PDE models

2.4.1 Finite difference method

Most of the PDEs described in the previous section can be written in the following general form:

$$\begin{cases} \dfrac{\partial I}{\partial t} = R\left(I, \dfrac{\partial I}{\partial x}, \dfrac{\partial I}{\partial y}, \dfrac{\partial^2 I}{\partial x^2}, \dfrac{\partial^2 I}{\partial y^2}, \dfrac{\partial^2 I}{\partial x \partial y}\right), & \text{for } t > 0,\ (x, y) \in \Omega, \\ I(x, y, 0) = I_0(x, y), & \text{for } (x, y) \in \Omega, \end{cases} \tag{2.1}$$

where R describes the relation between the successive derivatives of the image I with respect to x and y, and $I_0(x, y)$is the initial condition (original image).

The finite difference method (FDM) is particularly well-suited for the numerical resolution of PDEs in image processing. Its predominance is mainly due to the fact that the digital image is stored in a computer using a discrete representation, in which it is described by a finite set of points (pixels) arranged on a regular grid.

In order to solve the PDE (2.1), it is natural to consider the following discretization:

$$x_i = ih, \quad y_j = jh, \quad t^n = n\Delta t,$$

with $i \in \{0, 1, \ldots, M - 1\}$, $j \in \{0, 1, \ldots, N - 1\}$, and $n \in \{0, 1, \ldots, T - 1\}$.

Here, M and N correspond to the number of rows and columns in the image, respectively, h denotes the spatial distance between two pixels (in practice we take $h = 1$), Δt is the time discretization step, and T is the number of iterations required to reach the scale $t = \Delta t \cdot T$. The choice of Δt is based on two criteria:

1. The number of iterations required to perform the processing should not be very large, so Δt it must not be too small.

2. The numerical stability of the scheme, which requires that Δt must not be too large.

Thus, the function $I(x, y, t)$ is replaced by its discrete counterpart $I(x_i, y_j, t^n)$, denoted in index notation as $I^n_{i,j}$.

The explicit Euler scheme in time is often chosen because of its simple implementation and computational efficiency. It relies on approximating the time derivative using the forward finite difference:

$$\left.\frac{\partial I}{\partial t}\right|^n_{i,j} \approx \frac{I^{n+1}_{i,j} - I^n_{i,j}}{\Delta t}.$$

To approximate the spatial derivatives, a classical approach is to use centered finite differences. For first-order derivatives, this gives:

$$\left.\frac{\partial I}{\partial x}\right|^n_{i,j} \approx \frac{I^n_{i+1,j} - I^n_{i-1,j}}{2h}, \qquad \left.\frac{\partial I}{\partial y}\right|^n_{i,j} \approx \frac{I^n_{i,j+1} - I^n_{i,j-1}}{2h}. \tag{2.2}$$

Similarly, for second-order derivatives, we use the centered scheme:

$$\left.\frac{\partial^2 I}{\partial x^2}\right|^n_{i,j} \approx \frac{I^n_{i+1,j} - 2I^n_{i,j} + I^n_{i-1,j}}{h^2}, \qquad \left.\frac{\partial^2 I}{\partial y^2}\right|^n_{i,j} \approx \frac{I^n_{i,j+1} - 2I^n_{i,j} + I^n_{i,j-1}}{h^2}. \tag{2.3}$$

The mixed derivative is approximated by

$$\left.\frac{\partial^2 I}{\partial x \partial y}\right|^n_{i,j} \approx \frac{I^n_{i+1,j+1} - I^n_{i+1,j-1} - I^n_{i-1,j+1} + I^n_{i-1,j-1}}{4h^2}. \tag{2.4}$$

These finite difference approximations allow continuous differential operators to be replaced by discrete operators, making the PDE numerically solvable. For more details on numerical methods for solving PDEs in image processing, the reader is referred to [75].

2.4.2 Euler–Maruyama method

To handle the stochastic component, we employ the Euler–Maruyama method, which is the stochastic analogue of the classical Euler scheme. Given a stochastic differential equation of the form

$$dX_t = \mu(X_t, t)\, dt + \sigma(X_t, t)\, dW_t,$$

where X_t is the stochastic process, $\{W_t\}_{t\geq 0}$ be a d-dimentional Wiener process, μ and σ represent the drift and diffusion terms respectively, with initial condition $X(0) = X_0$.
The Euler–Maruyama approximation with time step Δt is given by

$$X_{n+1} = X_n + \mu(X_n, t_n)\, \Delta t + \sigma(X_n, t_n)\, \Delta W_n,$$

where $\Delta W_n \sim \mathcal{N}(0, \Delta t)$ represents increments of the Wiener process.
This method is particularly suitable for simulating stochastic image models, as it provides a balance between computational simplicity and accuracy. In our numerical implementation, the Euler–Maruyama scheme is combined with finite differences to approximate the evolution of the stochastic PDE model over discrete space and time grids.

2.5 Conclusion

This chapter establish the mathematical background for our study. We introduced functional spaces to ensure a rigorous framework for analyzing PDE-based image models and presented the stochastic framework as a tool to model uncertainty and noise. In addition, we outlined

the numerical methods, which will serve as the computational foundation of our implementations. Altogether, these preliminaries form the basis for developing the theory and numerical experimentations for image restoration in the next chapters.

Chapter 3

Stochastic differential equations in image restoration

3.1 Introduction

In this chapter, we highlight the growing role of stochastic differential equations (SDEs) in image processing [4], [5], [15], [16], [17], [26] and [27]. Their increasing mathematical relevance stems from the fundamental relationship between SDEs and partial differential equations (PDEs), where solutions to certain PDEs can be represented as expectations of stochastic processes through probabilistic tools such as Itô's formula and the Kolmogorov equations [42], [61] and [69]. This stochastic viewpoint provides greater flexibility and enables the incorporation of randomness to better model noise and local image variability.

We then introduce new SDE-based models for restoring noisy images. Our approach begins by revisiting two existing formulations: the model of Barbu et al. [5], which uses a unit diffusion coefficient, and the model of Borkowski et al. [15], which omits the drift term. By combining the strengths of both, and by integrating Perona–Malik diffusivity functions [63], we propose a unified SDE model that includes both drift and diffusion components.

Next, we establish the existence and uniqueness of solutions to the proposed stochastic models, ensuring their mathematical well-posedness. We then construct an Euler–Maruyama discretisation of the models and perform a comparative numerical study. The numerical experiments confirm that our method is effective in removing noise while preserving edges and important structures.

3.2 Foundations and related works

- **In 2016,** Barbu et al [5] presented the following SDE model

$$\begin{cases} dX(t) = \underbrace{\mu_1(X(t))}_{drift} dt + dW(t), \\ X(0,x,y) = X_0(x,y) \in \mathbb{R}^2, \end{cases} \tag{3.1}$$

  where:

  - the diffusion process $X(t) : \mathbb{R}^2 \longrightarrow \mathbb{R}^2$, i.e. $X(t) = \{X_1(t), X_2(t)\}$ represents a random variable, with: $|X(t)|^2 = X_1(t)^2 + X_2(t)^2$
  - $W(t) = \lambda\{\omega_1(t), \omega_2(t)\}$, $\lambda \in (0,1)$, represents a 2D Brownian motion in a probability space $\{\Omega, F, P\}$
  - $(F_t)_{t\geq 0}$ be the natural filtration
  - The drift term $\mu_1 : \mathbb{R}^2 \longrightarrow \mathbb{R}^2$ is Lipschitzian defined by

$$\mu_1(X(t)) = -\left(e^{-\alpha_1|X(t)|^2}, e^{-\alpha_2|X(t)|^2}\right), \qquad \alpha_1, \alpha_2 \geq 0 \tag{3.2}$$

  - $X_0(x,y)$ is a function defined on $\mathbb{R}^2$, corresponding to the initial image.

  Although this model provides satisfactory numerical results, the omission of geometric structures present in the image leads to an undesirable isotropic smoothing effect.

Notably, the authors proposed an efficient restoration model based on a PDE derived from the Kolmogorov equation associated with the underlying SDE (3.1), given by

$$\begin{cases} \dfrac{\partial u(t,\Psi)}{\partial t} = \dfrac{\eta^2}{2}\Delta_\Psi u(t,\Psi) - \mu(\Psi)\nabla_\Psi u(t,\Psi), t \geq 0 \\ u(0,\Psi) = u_0(\Psi), \qquad \Psi \in \mathbb{R}^2, \end{cases} \tag{3.3}$$

where, $\Psi = X_0(x,y) = \{i,j\}_{i=\overline{1,M},j=\overline{1,N}}$ and $\eta \in (0,1]$

- **In 2017,** Borkowski et al in [17] proposed the following SDE

$$\begin{cases} dX(t) = \underbrace{\sigma_1(X(t))}_{diffusion} dW(t), \\ X(0,x,y) = X_0(x,y) \in \mathbb{R}^2, \end{cases} \tag{3.4}$$

where $\sigma_1(X(t))$ is defined as

$$\sigma_1(X(t)) = \begin{pmatrix} -\dfrac{(G_\gamma * I)_y(X(t))}{|\nabla(G_\gamma * I)(X(t))|} & 0 \\ \dfrac{(G_\gamma * I)_x(X(t))}{|\nabla(G_\gamma * I)(X(t))|} & 0 \end{pmatrix} \tag{3.5}$$

The notation $(G_\gamma * I)$ refers to the convolution of the image I with a Gaussian smoothing kernel G_γ of standard deviation γ, typically implemented using a 3×3 mask to reduce sensitivity to noise. The partial derivatives $(G_\gamma * I)_x$ and $(G_\gamma * I)_y$ denote the first-order derivatives of the smoothed image with respect to x and y, respectively:

$$(G_\gamma * I)_x = \frac{\partial (G_\gamma * I)}{\partial x}, \quad (G_\gamma * I)_y = \frac{\partial (G_\gamma * I)}{\partial y}.$$

The Gaussian filter G_γ is defined as:

$$G_\gamma(x,y) = \frac{1}{2\pi\gamma^2} \exp\left(-\frac{x^2+y^2}{2\gamma^2}\right).$$

The expression of the diffusion matrix $\sigma(X(t))$ contributes to an anisotropic smoothing process that reduces noise while preserving edges. In Equation (3.4), we observe the initial absence of a drift term. However, several works emphasize that while the diffusion term plays a central role in controlling regularity and suppressing noise, it also leads to behavior strongly reminiscent of anisotropic diffusion techniques. Notably, Perona and Malik [63] demonstrate in their pioneering work that diffusion alone, when properly adapted, can effectively smooth images while preserving significant features such as edges. This highlights the importance of the diffusion structure in guiding the restoration process.

3.3 Proposed SDEs models

In this section, we propose SDE models that incorporate both drift and diffusion terms, in contrast to Barbu's model (3.1), which includes only the drift term with the diffusion coefficient set to 1, and Borkowski's approach (3.4), which focuses solely on the diffusion term while neglecting the drift. Here, we present several models based on three proposed forms of drift and diffusion terms, designed to analyze the impact of different configurations on image restoration quality. For each model, we provide the mathematical formulation, study the well-posedness of the associated SDE, and develop a corresponding numerical implementation for practical image denoising.

The general form of the SDE is expressed as follows:

$$\begin{cases} dX(t) = \underbrace{\mu_k(X(t))}_{drift}dt + \underbrace{\sigma_k(X(t))}_{diffusion}dW_t, \quad k = \overline{1,3} \\ X(0,x,y) = X_0(x,y) \in \mathbb{R}^2 \end{cases} \tag{3.6}$$

Where $X(t)$ is the stochastic process and the associated solution is given by

$$X(t) = X_0 + \int_0^t \mu_k(X(s))ds + \int_0^t \sigma_k(X(s))dW(s). \tag{3.7}$$

The restored image is defined by

$$u(x, y) = E[u_0(X_T)] = \frac{1}{M}\sum_{i=1}^{M} u_0(X_T^m(\beta_i)), \tag{3.8}$$

where $u_0 : \mathbb{R}^2 \to \mathbb{R}$, the noisy image, $X_T^m(\beta_i)$ the trajectory approximation for the stochastic process $X(t)$, here m, T and β_i denote the m^{th} iteration, the final time and the random variable, respectively, whereas M is the number of Monte Carlo's iterations.

In the following sections, we introduce our proposed SDEs models, with different choices for the drift μ_k and diffusion terms σ_k.

3.3.1 First SDE model

In the fist proposed model, we combine the drift term introduced by Barbu (3.2) with the anisotropic stochastic diffusion term from Borkowski's work (3.5). The proposed model is given by the following equation:

$$X(t) = X_0 + \int_0^t \mu_1(X(s))ds + \int_0^t \sigma_1(X(s))dW(s), \quad t \in [0, T] \tag{3.9}$$

Barbu's (3.2) drift formulation is designed to guide the evolution of the restoration process in a deterministic and feature-aware direction, helping to preserve important image structures while suppressing noise. His model, derived from a Kolmogorov-type PDE associated with an SDE [5], ensures well-posedness and allows for a stable numerical scheme, particularly suitable for handling noisy data in a controlled manner. On the other hand, Borkowski's diffusion term

(3.5), which is highly adaptive and anisotropic, effectively smooths the image by diffusing along directions of low intensity variation while preserving sharp edges. This is achieved by using a structure-sensitive diffusion coefficient based on gradients of a Gaussian-smoothed version of the image. By integrating these two complementary elements Barbu's deterministic structural guidance through drift and Borkowski's stochastic anisotropic diffusion, we aim to provide a balanced restoration while ensuring robust noise reduction.

3.3.2 Existence and uniqueness

In this section, we investigate the existence and uniqueness of our proposed SDEs models. We use Øksendal's theorem [61],

Theorem 3.3.1. Let $t \in [0,T]$ and $\{W_t\}_{t\geq 0}$ be a d-dimensional Brownian motion defined on a probability space $(\Omega, \mathcal{F}, \mathbb{P})$ with its natural filtration $\{\mathcal{F}_t\}_{t\geq 0}$. Consider the stochastic differential equation:

$$dX(t) = \mu(t, X(t))\, dt + \sigma(t, X(t))\, dW(t), \tag{3.10}$$

where, $\mu : [0,T] \times \mathbb{R}^d \to \mathbb{R}^d, \quad \sigma : [0,T] \times \mathbb{R}^d \to \mathbb{R}^{d\times d'}$ are measurable functions satisfying the following conditions:

1. Lipschitz condition: $\exists$ a constant $M_1 > 0$ such that

$$|\mu(t,X) - \mu(t,Y)| + |\sigma(t,X) - \sigma(t,Y)| \leq M_1|X-Y|, \forall t \in [0,T], \forall X, Y \in \mathbb{R}^d. \tag{3.11}$$

2. Linear growth condition: $\exists$ a constant $M_2 > 0$ such that

$$|\mu(t,X)| + |\sigma(t,X)| \leq M_2(1+|X|), \quad \forall t \in [0,T], \forall X \in \mathbb{R}^d. \tag{3.12}$$

Let $Y = X_0$ be a random variable independent of the σ-algebra generated by $\{W_s\}_{s\geq 0}$, and suppose $\mathbb{E}|Y|^2 < \infty$. Then the SDE (3.10) has a unique solution $X(t)$, adapted to the

filtration $\{\mathcal{F}_t^Y\}$, and it satisfies: $\mathbb{E}\int_0^T |X(t)|^2\,dt < \infty$.

Let us adopt this result in the proposed model, i.e. (3.10) together with (3.2) and (3.5).

To prove this theorem, In the first instance, we consider equation (3.10) with $X_0 = \{i,j\}_{i=1....M,j=1.....N}$ representing the pixel positions of the original image of size $M \times N$, which evidently fulfills the requirement stated in condition $\mathbb{E}|Y|^2 < \infty$.
Then, If we use (3.2) and (3.5) for μ_1 and σ_1 , respectively, we get

$$\begin{aligned}
|\mu_1(t,X)|^2 &= \left(e^{-\alpha_1|X|^2}\right)^2 + \left(e^{-\alpha_2|X|^2}\right)^2 \\
&\leq 2\alpha_1|X|^2 + 2\alpha_2|X|^2, \\
&= 2(\alpha_1+\alpha_2)|X|^2, \\
&\leq 4\alpha|X|^2,\ \forall \alpha_1,\alpha_2 > 0, X \in \mathbb{R}^2,\ t \in [0,T],
\end{aligned}$$

with $\alpha = max(\alpha_1,\alpha_2)$. Hence

$$|\mu_1(t,X)| \leq 2\sqrt{\alpha}|X| + 2\sqrt{\alpha} \leq 2\sqrt{\alpha}(1+|X|).. \tag{3.13}$$

For simplicity, we denote $(G_\gamma * I)(X)$ by $F(X)$ in the following

$$\begin{aligned}
|\sigma_1(t,X)|^2 &= \left(-\frac{F_y(X)}{|\nabla F(X)|}\right)^2 + \left(\frac{F_x(X)}{|\nabla F(X)|}\right)^2 \\
&= \frac{(F_y(X))^2}{(F_x(X))^2 + (F_y(X))^2} + \frac{(F_x(X))^2}{(F_x(X))^2 + (F_y(X))^2} \\
&= \frac{(F_y(X))^2 + (F_x(X))^2}{(F_x(X))^2 + (F_y(X))^2} \\
&= 1.
\end{aligned}$$

Hence

$$|\sigma_1(t,X)| \leq 1 + |X|, \forall X \in \mathbb{R}^2., \tag{3.14}$$

From (3.13) and (3.14) we obtain

$$\begin{aligned} |\mu_1(t,X)| + |\sigma_1(t,X)| &\leq 2\sqrt{\alpha}(1+|X|) + (1+|X|) && (3.15)\\ &= (2\sqrt{\alpha}+1)(1+|X|) && (3.16)\\ &\leq M_1(1+|X|). && (3.17) \end{aligned}$$

with $M_1 = 2\sqrt{\alpha}+1$. This proves the condition (3.12).

In the same way we use (3.2) and (3.5) for μ_1 and σ_1 , respectively and get

$$\begin{aligned} |\mu_1(t,X) - \mu_1(t,Y)|^2 &= \left(e^{-\alpha_1|X|^2} - e^{-\alpha_1|Y|^2}\right)^2 \\ &\quad + \left(e^{-\alpha_2|X|^2} - e^{-\alpha_2|Y|^2}\right)^2 \\ &\leq \alpha_1|X|^2 - \alpha_1|Y|^2 + \alpha_2|X|^2 - \alpha_2|Y|^2 \\ &= (\alpha_1+\alpha_2)|X|^2 - (\alpha_1+\alpha_2)|Y|^2 \\ &= (\alpha_1+\alpha_2)(|X|^2 - |Y|^2) \\ &\leq 4\alpha\left(|X| - |Y|\right)\left(|X| + |Y|\right) \\ &\leq 4\alpha K\left(|X-Y|\right) \end{aligned}$$

with $\alpha = max(\alpha_1, \alpha_2) > 0$, and $K = |X| + |Y|$.

Hence

$$|\mu_1(t,X) - \mu_1(t,Y)| \leq 2\sqrt{\alpha K}|X-Y|. \tag{3.18}$$

$$|\sigma_1(t,X) - \sigma_1(t,Y)|^2 = \left(-\frac{F_y(X)}{|\nabla F(X)|} + \frac{F_y(Y)}{|\nabla F(Y)|}\right)^2 + \left(\frac{F_x(X)}{|\nabla F(X)|} - \frac{F_x(Y)}{|\nabla F(Y)|}\right)^2$$

$$
\begin{aligned}
|\sigma_1(t,X)-\sigma_1(t,Y)|^2 &= \left(\frac{F_y(X)}{|\nabla F(X)|}\right)^2+\left(\frac{F_y(Y)}{|\nabla F(Y)|}\right)^2-2\frac{F_y(X)}{|\nabla F(X)|}.\frac{F_y(Y)}{|\nabla F(Y)|} \\
&\quad +\left(\frac{F_x(X)}{|\nabla F(X)|}\right)^2+\left(\frac{F_x(Y)}{|\nabla F(Y)|}\right)^2-2\frac{F_x(X)}{|\nabla F(X)|}.\frac{F_x(Y)}{|\nabla F(Y)|} \\
&\leq (F_y(X))^2+(F_y(Y))^2+(F_x(X))^2+(F_x(Y))^2 \\
&\quad -2\left(F_y(X)F_y(Y)\right)-2\left(F_x(X)F_x(Y)\right) \\
&\leq (\nabla F(X))^2+(\nabla F(Y))^2-2\left(\nabla F(X)\nabla F(Y)\right) \\
&= \left(\nabla F(X)-\nabla F(Y)\right)^2. \qquad (3.19)
\end{aligned}
$$

Given that F(X) is a differentiable function within a convex set, there exists a positive constant L such that $\nabla F(X)$ is lipschitzian.

the inequality (3.19) can be formulated as

$$|\sigma_1(t,X)-\sigma_1(t,Y)|\leq L|X-Y|. \qquad (3.20)$$

From (3.18) and (3.20) we obtain,

$$
\begin{aligned}
|\mu_1(t,X)-\mu_1(t,Y)|+|\sigma_1(t,X)-\sigma_1(t,Y)| &\leq 2\sqrt{\alpha K}|X-Y|+L|X-Y| \\
&\leq M_2\left|X-Y\right|, \qquad (3.21)
\end{aligned}
$$

with $M_2=2\sqrt{\alpha K}+L$.

From (3.17) and (3.21), we conclude that the proposed model has a unique solution.

3.3.3 Second SDE model

In this model, we exploit the PM functions together with the drift and diffusion terms proposed by Barbu and Borkowski, while modifying their formulation by substituting the deterministic pixel value $u(x_i,y_j)$ with a random variable $X(i,j)$. Based on this framework,

we propose four different cases of stochastic modeling:

- **Case 1:** We consider equation (3.6) with the PM functions as drift terms, given by

$$\mu_2(X(t)) = \left(e^{-\frac{|\nabla X(t)|^2}{k_1^2}},\ e^{-\frac{|\nabla X(t)|^2}{k_2^2}} \right), \tag{3.22}$$

  or alternatively,

$$\mu_3(X(t)) = \left(\frac{1}{1+\frac{|\nabla X(t)|^2}{k_1^2}},\ \frac{1}{1+\frac{|\nabla X(t)|^2}{k_2^2}} \right), \tag{3.23}$$

  together with the Borkowski diffusion term (3.5).

- **Case 2:** We consider equation (3.6) with Barbu's drift term (3.2) combined with PM diffusion terms, expressed as

$$\sigma_2(X(t)) = \begin{pmatrix} -e^{-\frac{|\nabla (G_\gamma * I)(X(t))|^2}{k_1^2}} & 0 \\ e^{-\frac{|\nabla (G_\gamma * I)(X(t))|^2}{k_2^2}} & 0 \end{pmatrix}, \tag{3.24}$$

  or alternatively,

$$\sigma_3(X(t)) = \begin{pmatrix} -\frac{1}{1+\frac{|\nabla (G_\gamma * I)(X(t))|^2}{k_1^2}} & 0 \\ \frac{1}{1+\frac{|\nabla (G_\gamma * I)(X(t))|^2}{k_2^2}} & 0 \end{pmatrix}, \tag{3.25}$$

  with parameters $k_1, k_2 > 0$.

- **Case 3:** We consider equation (3.6) with the drift terms given by (3.22) or (3.23), and set the diffusion term to a constant value $\sigma = 1$.

- **Case 4:** We consider equation (3.6) with vanishing drift ($\mu = 0$) and diffusion terms defined by (3.24) or (3.25).

The rationale for adopting decreasing functions of the gradient magnitude as drift and

diffusion terms lies in their ability to suppress noise while preserving important image structures. High gradient values are typically associated with edges or fine details, where smoothing should be minimized to maintain structural information, whereas low gradient values correspond to homogeneous regions where noise reduction is more appropriate. The parameters $\mathbf{k_1}$ and $\mathbf{k_2}$ regulate the sensitivity of the model to gradient variations: smaller values enhance edge preservation by reducing smoothing near sharp transitions, while larger values promote more uniform denoising across the image.

By incorporating both Barbu's drift and Borkowski's diffusion in combination with the Perona–Malik functions, the four proposed cases offer different balances between edge preservation and noise attenuation. In particular, the use of Gaussian convolution G_γ in the diffusion terms introduces a multiscale effect that further improves robustness against high-frequency noise. Moreover, by modeling pixel intensities as random variables rather than deterministic values, the stochastic formulation explicitly accounts for uncertainty in the data, which enhances stability and enables better recovery of fine image structures under noisy conditions. This unified framework thus provides a versatile approach to explore the impact of different drift–diffusion interactions in stochastic image restoration.

3.3.4 Existence and uniqueness

In this part, we investigate the well-posedness of the case 1 (i.e. a drift defined by (3.22) with Borkowski's diffusion (3.5)).

Theorem 3.3.2. Assume that all the conditions of Theorem 3.3.1 hold then (4.12) have a unique solution.

Proposition 3.3.3. Let μ_2 and σ_1 be defined by (3.22) and (3.5), respectively, then

$$|\mu_2(t,X)| + |\sigma_1(t,X)| \leq C_1(1+|X|), \quad C_1 > 0. \tag{3.26}$$

Proof. We have μ and σ defined by (3.22) and (3.5), respectively

$$\begin{aligned} |\mu_2(t,X)|^2 &= \left(e^{-(\frac{|\nabla X|^2}{k_1^2})}\right)^2 + \left(e^{-(\frac{|\nabla X|^2}{k_2^2})}\right)^2 \\ &\leq 2. \end{aligned}$$

From (4.35), we have $|\sigma_1(t,X)| = 1$.

Hence

$$|\mu_2(t,X)| + |\sigma_1(t,X)| \leq \sqrt{2} + 1.$$

This implies that there exists $C_1 > 0$ which satisfies the following relation

$$|\mu_2(t,X)| + |\sigma_1(t,X)| \leq C_1(1 + |X|), \quad C_1 > 0. \tag{3.27}$$

□

So the condition (3.12) holds.

Proposition 3.3.4. Let μ_2 and σ_1 defined by (3.22) and (3.5), then we have

$$|\mu_2(t,X) - \mu_2(t,Y)| + |\sigma_1(t,X) - \sigma_1(t,Y)| \leq C_2|X - Y|. \tag{3.28}$$

Proof. If μ_2 and σ_1 are given by (3.22) and (3.5), respectively, we write

$$\begin{aligned}
|\mu_2(t,X)-\mu_2(t,Y)|^2 &= \left(e^{-(\frac{|\nabla X|^2}{k_1^2})}-e^{-(\frac{|\nabla Y|^2}{k_1^2})}\right)^2 \\
&+ \left(e^{-(\frac{|\nabla X|^2}{k_2^2})}-e^{-(\frac{|\nabla Y|^2}{k_2^2})}\right)^2 \\
&\leq \left(e^{-(\frac{|\nabla X|^2}{k_1^2})}\right)^2+\left(e^{-(\frac{|\nabla Y|^2}{k_1^2})}\right)^2 \\
&+ \left(e^{-(\frac{|\nabla X|^2}{k_2^2})}\right)^2+\left(e^{-(\frac{|\nabla Y|^2}{k_2^2})}\right)^2 \\
&\leq 4,
\end{aligned}$$

i.e.

$$|\mu_2(t,X)-\mu_2(t,Y)|\leq 2.$$

In the same way we prove that

$$|\mu_2(t,X)-\mu_2(t,Y)|+|\sigma_1(t,X)-\sigma_1(t,Y)|\leq C_2|X-Y|. \tag{3.29}$$

This yields that the proposed model (case 1) has a unique solution. □

Remark 3.3.5. The proofs of the other cases proceed in the same manner.

3.4 Discretisation and numerical study

In this section, we present the discretization of the proposed model together with its numerical study. The construction of an appropriate numerical scheme is essential to ensure both the stability and the accuracy of the solution. We first detail the discretization process, highlighting the choices made for time and spatial approximations. Then, we analyze the stability of the scheme to guarantee its reliability. Finally, we provide experimental results

that illustrate the effectiveness of the proposed approach in practice.

3.4.1 Numerical implementation

To discretize (3.6), we use Euler's Maruyama numerical scheme and obtain

$$\begin{cases} X^m_{t_{n+1}}(i,j) = X^m_{t_n}(i,j) + \Delta t\left(\mu_k(X^m_{t_n}(i,j)) + \sigma_k(X^m_{t_n}(i,j))(w^{n+1}_{i,j} - w^n_{i,j})\right), k = \overline{1,3} \\ X^m_0(i,j) = X_0(i,j), i = \overline{1,M},\ j = \overline{1,N}, \end{cases} \tag{3.30}$$

where $t_n = n\Delta t$, $\Delta t = \frac{T}{m}$, $n = 0, 1, .., m$ with m the number of $t-$iterations, and

$$w^n_{i,j} = w(n\Delta t, x_i, y_j),$$

with $x_i = i\Delta x$ and $y_j = j\Delta y$.

The drift and diffusion terms are approximated by

$$\mu_1(X^m_{t_n}(i,j)) = -\left(e^{-\alpha_1((X^m_{1,n,i,j})^2+(X^m_{2,n,i,j})^2)}, e^{-\alpha_2((X^m_{1,n,i,j})^2+(X^m_{2,n,i,j})^2)}\right) \tag{3.31}$$

$$\mu_2(X^m_{t_n}(i,j)) = -\left(e^{-\left(\frac{(X^m_{n,i+1,j}-X^m_{n,i-1,j})^2+(X^m_{n,i,j+1}-X^m_{n,i,j-1})^2}{4k_1^2}\right)}, e^{-\left(\frac{(X^m_{n,i+1,j}-X^m_{n,i-1,j})^2+(X^m_{n,i,j+1}-X^m_{n,i,j-1})^2}{4k_2^2}\right)}\right) \tag{3.32}$$

$$\mu_3(X^m_{t_n}(i,j)) = -\left(\frac{1}{1+\left(\frac{(X^m_{n,i+1,j}-X^m_{n,i-1,j})^2+(X^m_{n,i,j+1}-X^m_{n,i,j-1})^2}{4k_1^2}\right)}, \frac{1}{1+\left(\frac{(X^m_{n,i+1,j}-X^m_{n,i-1,j})^2+(X^m_{n,i,j+1}-X^m_{n,i,j-1})^2}{4k_2^2}\right)}\right) \tag{3.33}$$

and

$$\sigma_1(X^m_{t_n}(i,j)) = \begin{pmatrix} -\frac{(u^n_{i,j+1}+u^n_{i,j-1})*0.5}{\sqrt{\left(\frac{u^n_{i+1,j}+u^n_{i-1,j})}{2}\right)^2+\left(\frac{u^n_{i,j+1}+u^n_{i,j-1}}{2}\right)^2}} & 0 \\ \frac{(u^n_{i+1,j}+u^n_{i-1,j})*0.5}{\sqrt{\left(\frac{u^n_{i+1,j}+u^n_{i-1,j})}{2}\right)^2+\left(\frac{u^n_{i,j+1}+u^n_{i,j-1}}{2}\right)^2}} & 0 \end{pmatrix}, \tag{3.34}$$

$$\sigma_2(X_{t_n}^m(i,j)) = \begin{pmatrix} -e^{-\frac{\left(\frac{u_{i+1,j}^n+u_{i-1,j}^n}{2}\right)^2+\left(\frac{u_{i,j+1}^n+u_{i,j-1}^n}{2}\right)^2}{k_1^2}} & 0 \\ e^{-\frac{\left(\frac{u_{i+1,j}^n+u_{i-1,j}^n}{2}\right)^2+\left(\frac{u_{i,j+1}^n+u_{i,j-1}^n}{2}\right)^2}{k_2^2}} & 0 \end{pmatrix} \tag{3.35}$$

$$\sigma_3(X_{t_n}^m(i,j)) = \begin{pmatrix} -\frac{1}{1+\frac{(u_{i+1,j}^n+u_{i-1,j}^n)^2+(u_{i,j+1}^n+u_{i,j-1}^n)^2}{4k_1^2}} & 0 \\ \frac{1}{1+\frac{(u_{i+1,j}^n+u_{i-1,j}^n)^2+(u_{i,j+1}^n+u_{i,j-1}^n)^2}{4k_2^2}} & 0 \end{pmatrix} \tag{3.36}$$

here, the space steps $\Delta x = \Delta y = 1$, with

$$\begin{cases} (G_\gamma * u_0)_y = u_y = (u(i,j+1) + u(i,j-1)) * 0.5, \\ (G_\gamma * u_0)_x = u_x = (u(i+1,j) + u(i-1,j)) * 0.5. \end{cases}$$

3.4.2 Stability analysis

In this subsection, we present a numerical stability analysis for the numerical scheme (3.30).

Definition 3.1. Scheme (3.30) said to be stable, if there exists a constant C such that

$$|X_{t_{n+1}}^m(i,j) - X_{t_n}^m(i,j)| \leq C\Delta t. \tag{3.37}$$

Let us find the stability condition for (3.30), i.e. find C in (3.37) explicitly.

Proposition 3.4.1. If hypotheses (3.32) and (3.34) satisfy the properties of μ and σ, respectively, then

$$|X_{t_{n+1}}^m(i,j) - X_{t_n}^m(i,j)| \;\leq\; \Delta t\left(\sqrt{2} + \varepsilon_n(i,j)\right), \tag{3.38}$$

with $\varepsilon_n(i,j) > 0$.

Proof. To prove (3.37), we write

$$X^m_{t_{n+1}}(i,j) - X^m_{t_n}(i,j) = \Delta t \left[\mu(X^m_{t_n}(i,j)) + \sigma(X^m_{t_n}(i,j)).(w^{n+1}_{i,j} - w^n_{i,j})\right], \tag{3.39}$$

we apply the Euclidean norm $|.|$ on both sides of (3.39), to obtain

$$\begin{aligned} |X^m_{t_{n+1}}(i,j) - X^m_{t_n}(i,j)| &= |\Delta t \left[\mu(X^m_{t_n}(i,j)) + \sigma(X^m_{t_n}(i,j))(w^{n+1}_{i,j} - w^n_{i,j})\right]| \\ &\leq |\Delta t| \left[|\mu(X^m_{t_n}(i,j))| + |\sigma(X^m_{t_n}(i,j))|\varepsilon_n\right], \end{aligned} \tag{3.40}$$

where

$$\varepsilon_n = \varepsilon_n(i,j) = |(w^{n+1}_{i,j} - w^n_{i,j})|.$$

If we replace μ and σ by (3.32) and (3.34), respectively, we get

$$|\mu(X^m_{t_n}(i,j))| \leq \sqrt{2}, \tag{3.41}$$

and

$$|\sigma(X^m_{t_n}(i,j))| = 1. \tag{3.42}$$

By substituting (3.41) and (3.42) in (3.40), we obtain

$$\begin{aligned} |X^m_{t_{n+1}}(i,j) - X^m_{t_n}(i,j)| &\leq \Delta t \left(\sqrt{2} + \varepsilon_n(i,j)\right) \\ &\leq C\Delta t \leq 1, \qquad C > 0, \Delta t > 0, \end{aligned}$$

leading to the following stability condition

$$\Delta t \leq \frac{1}{C},\ C = \sqrt{2} + \varepsilon_n(i,j) > 0, \tag{3.43}$$

for an appropriate choice of Δt to solve (3.30). □

The other cases are proved in the same way.

3.4.3 Numerical results and comments

This section presents the numerical results and related comments. We consider a noisy image and apply the SDE models described in the previous sections, using different values for the variance γ.

First experimentations: we explored the following cases for
$\gamma = 0.01$ and 0.1

1. PM-Borkowski: Borkowski's diffusion with PM-functions as drift term.
2. Barbu-PM: PM-functions as diffusion term and Barbu's drift term.
3. Barbu-Borkowski: Barbu's drift term and Borkowski's diffusion

Results are resumed in Table 3.1.

Second experimentations: we explored the following case for
$\gamma = 0.01$

- C1 (Case 1): Barbu's drift with Borkowski's diffusion in (3.6).
- C2 (Case 2): PM-functions as a diffusion term with Barbu's drift.
- C3 (Case 3): Borkowski's diffusion with PM-functions as a drift term.
- C4 (Case 4): PM-functions as a diffusion term and drift term = 0.
- C5 (Case 5): PM-functions as a drift term with diffusion = 1.
- Kolmogorov PDE: Barbu's associated PDE [5] .

The obtained results are resumed in Table 3.2 & 3.3. and Figure 3.1, 3.2 & 3.3

Variance	Model	SSIM	PSNR
0.1	Barbu	0.6257	23.6841
	Borkowski	0.5302	22.9435
	PM-Borkowski	**0.7847**	**23.8949**
	Barbu-Borkowski	0.5754	23.0245
	Barbu-PM	**0.8014**	**24.5376**
0.01	Barbu	0.8755	30.6092
	Borkowski	0.8557	30.2688
	PM-Borkowski	**0.9780**	**35.7153**
	Barbu-Borkowski	0.9051	32.1237
	Barbu-PM	**0.9871**	**38.6142**

Table 3.1: **PSNR** and **SSIM** values for different values of the variance with $\Delta t = 0.1$, $T = 1$.

Models	Barbu	Borkowski	C1	C2 (σ_1)	C2 (σ_2)	C3 (μ_1)
PSNR	30.6123	30.2688	32.2114	38.6125	38.5412	35.7283
SSIM	0.8746	0.8625	0.9022	0.9875	0.9820	0.9686
Models	C3 (μ_2)	C4 (σ_1)	C4 (σ_2)	C5 (μ_1)	C5 (μ_2)	PDE
PSNR	35.6909	29.2331	29.2691	29.8776	29.9572	23.0411
SSIM	0.9691	0.8488	0.8525	0.8688	0.8649	0.6511

Table 3.2: **PSNR** and **SSIM** values using different approaches for $\gamma = 0.01$, $\Delta t = 0.1$, $T = 1$, $M = 12$.

Models	PM 1	PM 2	Barbu	Borkowski	C1	C2 (σ_1)	C2 (σ_2)
PSNR	27.4508	27.6078	30.6202	30.1778	32.1417	38.5159	38.6181
SSIM	0.8580	0.8608	0.8743	0.8735	0.9854	0.9869	0.9779
Models	C3 (μ_1)	C3 (μ_2)	C4 (σ_1)	C4 (σ_2)	C5 (μ_1)	C5 (μ_2)	PDE
PSNR	35.7369	35.7744	29.4182	29.2514	29.8761	29.7959	23.1026
SSIM	0.8685	0.8695	0.8520	0.8486	0.8675	0.8635	0.6562

Table 3.3: **PSNR** and **SSIM** values using different approaches for $\gamma = 0.01$, $\Delta t = 0.5$, $T = 10$, $M = 12$

Comments

In this section, we compare the obtained numerical results. We applied the proposed model (3.6) with different expressions for diffusion σ and drift μ terms. The discretisation parameters used for our numerical implementations are, stopping time $T = 1$ & 10, step time $\Delta t = 0.1$ & 0.5 , number of iterations $M = 12$, $\alpha_1 = 2$, $\alpha_2 = 4$, $k_1 = 20$ and $k_2 = 40$.

As illustrated in Tables 3.1., 3.2. & 3.3., and Figure 3.1. & 3.2., we note that the proposed models ((3.6) together with (3.22) or (3.23), (3.24) or (3.25)) exhibit strong performance in both noise removal and the preservation of essential image features (such as edges, texture, curvature, etc..), compared to the combined Barbu-Borkowski SDE (Borkowski's diffusion and Barbu's drift terms). The two cases are largely comparable; however, the results obtained in the second case where Barbu's drift and Perona-Malik functions are used for the drift and diffusion terms, respectively offer a modest enhancement over those of the first case.
Table 3.1., 3.2 & 3.3. and Figure 3.1. & 3.2. give the numerical findings in terms of the Peak Signal to Noise Ratio (PSNR) and Structure Similarity Index Measure (SSIM) on a greyscale picture that has been modified by Gaussian white noise with a mean of zero and variance of $\gamma = 0.1$ & 0.01.

We have studied a comparison of the 5 cases for (3.6), and conclude that: - All SDEs

cases give better results compared to PDEs based models.

- Case 2 (σ_1 & σ_2) provides the best performance, demonstrating both strong numerical accuracy and excellent structural preservation compared to the other models.

- Case 1 achieves competitive results, outperforming Barbu's and Borkowski's models, although its performance remains below that of case 2.

- Case 3 (μ_1 & μ_2) yields improved results over Cases 1, 4, and 5, highlighting the suitability of the chosen drift and diffusion terms.

- Cases 4 & 5, are explored in a such way that PM-functions are used either for the diffusion or drift terms together with the Barbu's drift (3.2) and Borkowski's diffusion (3.5). In order to extract the inconveniences of these models when neglecting one of the terms, we note that we get better values for PSNR and SSIM.

3.5 Conclusion

In this work, we proposed a model that uses stochastic processes to restore images. The use of both terms (drift and diffusion) in SDE (3.6) aims to eliminate noise without sacrificing essential features or introducing false ones. The diffusion and drift terms have been adapted to better reflect the complexity of the geometric structures. Based on the numerical results obtained, we conclude that, in comparison to the combined Barbu-Borkowski SDE, our proposed models are generally more qualitatively efficient. This can be observed both visually, as in Figure 3.1, 3.2, 3.3 and 3.4, and quantitatively through the PSNR and SSIM metrics, as shown in Tables 3.1, 3.2 and 3.3. It is worth noting that the proposed models are also more intuitively realistic, producing encouraging numerical results in terms of noise removal and feature preservation when compared to PDE-based models. Furthermore, these models can be very promising for image inpainting [9] and [60].

Figure 3.1: Restored image results for different cases with $\mathbf{\Delta t} = 0.1$, $\gamma = 0.01$, $\mathbf{T} = 1$, $\mathbf{M} = 12$.

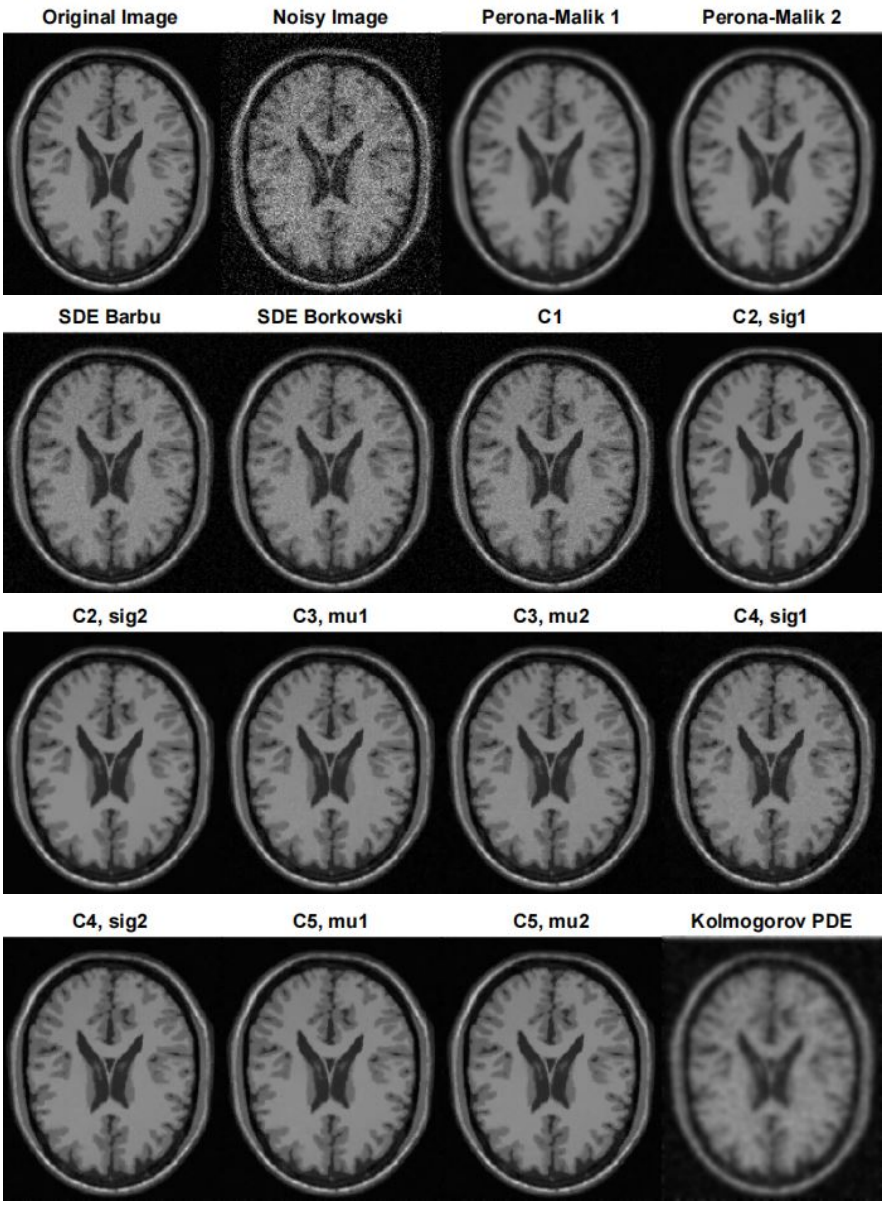

Figure 3.2: Restored image results for different cases with $\mathbf{\Delta t} = 0.5$, $\gamma = 0.01$, $\mathbf{T} = 10$, $\mathbf{M} = 12$.

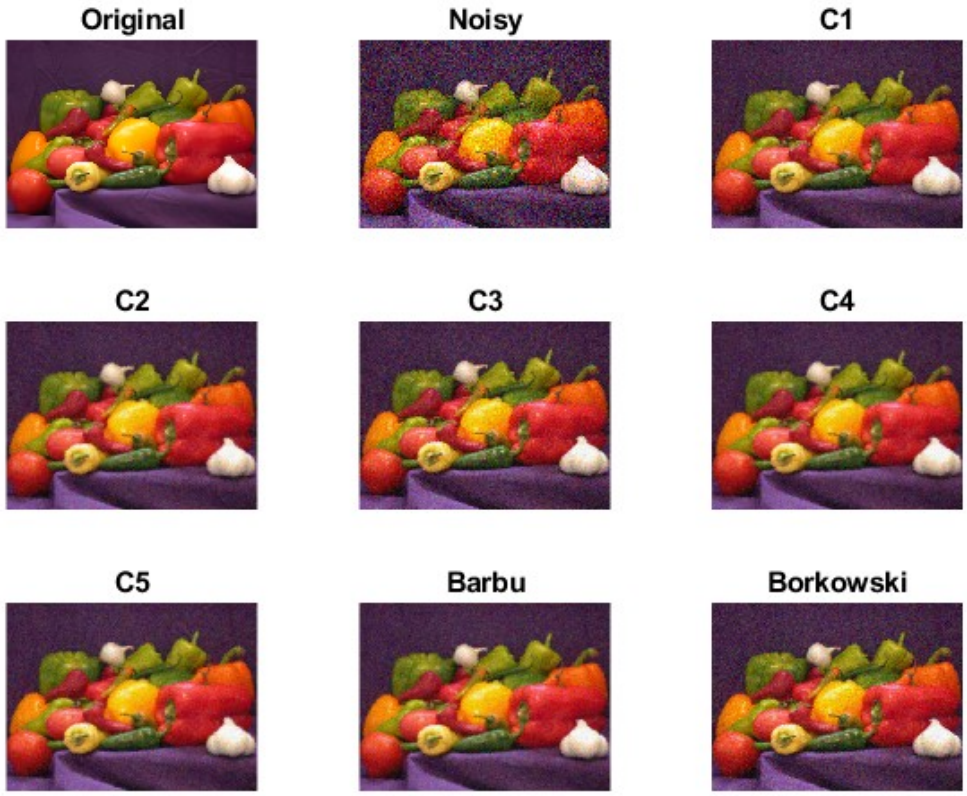

Figure 3.3: Restored color image results for different cases with $\mathbf{\Delta t} = 0.5$, $\gamma = 0.01$, $\mathbf{T} = 10$, $\mathbf{M} = 12$.

The zoomed regions (**Figure 3.4**) of interest highlight the effectiveness of the proposed model in suppressing noise while preserving edges and fine structural details.

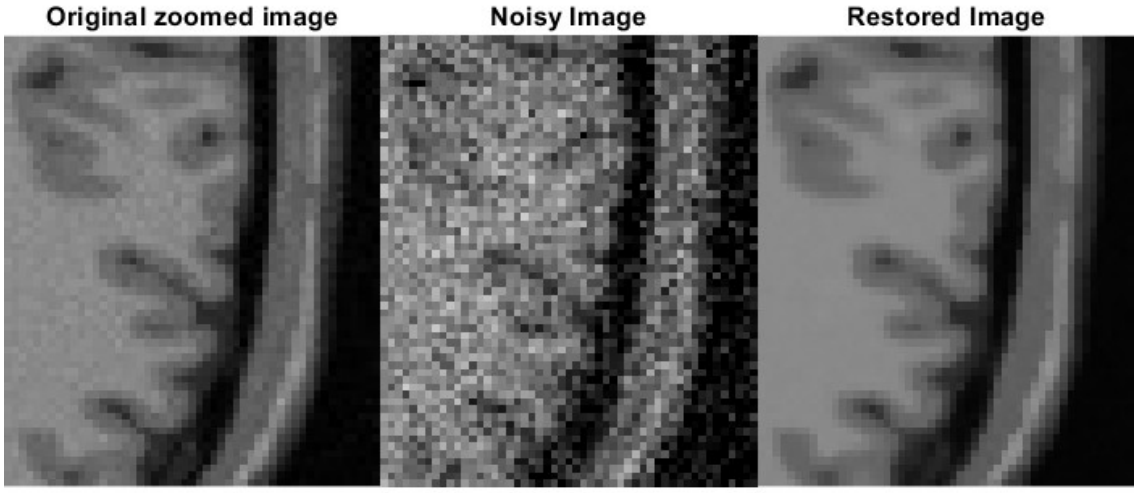

Figure 3.4: Visual comparison of the original, noisy, and restored images (case 2) with $\mathbf{\Delta t} = 0.5$, $\gamma = 0.01$, $\mathbf{T} = 10$, $\mathbf{M} = 12$.

Chapter 4

Stochastic partial differential equation in image denoising

4.1 Introduction

In this chapter, we address the problem of image restoration through a stochastic partial differential equation (SPDE) model that integrates anisotropic diffusion with Brownian motion. The combination of anisotropic diffusion and stochastic perturbations allows the model to effectively reduce noise while preserving important image features such as edges and textures. We investigate the existence and uniqueness of solutions under appropriate mathematical conditions and propose a finite difference scheme for the numerical resolution of the model. Furthermore, we conduct a stability analysis of the scheme using Fourier techniques. Numerical experiments confirm the effectiveness of the proposed approach and highlight its competitiveness compared to existing methods based on stochastic or deterministic PDEs.

4.2 Proposed model

In this section, we used a SBM to perturb a regularized PDE of PM [63] proposed by F. Catté, P.L. Lions, J.M. Morel and T. Coll [20], the problem can be written as follows

$$\begin{cases} \frac{\partial u}{\partial t} = div\left(g(|\nabla G_\sigma * u|)\nabla u\right) + dW_t \quad in \quad]0,T[\times D \times \Omega, \\ u(0,x) = u_0(x), \forall x \in D. \end{cases} \tag{4.1}$$

with

$$g(|\nabla G_\sigma * u|) = e^{-\frac{|\nabla G_\sigma * u|^2}{k^2}} \quad or \quad g(|\nabla G_\sigma * u|) = \frac{1}{1+\frac{|\nabla G_\sigma * u|^2}{k^2}}, \qquad k > 0. \tag{4.2}$$

In the problem (4.1) we have the following denotes

- $u_0 : D \subset \mathbb{R}^2 \to \mathbb{R}$ be the initial image.
- $D \subset \mathbb{R}^2$ is a Bounded domain with Lipschitz boundary and $0 < T < \infty$.
- G_σ is a Gaussian filter, $G_\sigma(x) = \frac{1}{\sqrt{2\pi\sigma}} exp\left(-\frac{|x|^2}{4\sigma}\right), \quad \sigma > 0, \quad x = (x_1, x_2) \in \mathbb{R}^2$.
- $(\Omega, \mathcal{F}, \mathcal{P})$ A completely regular topological space equipped with its Borel σ-algebra $\mathcal{F}$, and $\mathcal{P}$ is a Radon probability measure (i.e., an abstract measure on $\mathcal{F}$ that is inner regular) [55], [67].
- W_t be a Wiener process defined on $(\Omega, \mathcal{F}, \mathcal{P})$ and taking values in the separable Hilbert space H, with incremental covariance operator w. Let $(\mathcal{F}_t)_{t>0}$ be the σ-algebra generated by $W_s, 0 \leq s \leq t$ then W_t is a martingale relative to $(\mathcal{F}_t)_{t\geq 0}$ and we have the following representation of W_t :

$$W_t = \sum_{i=1}^{\infty} \beta_t^i e_i,$$

where e_i is an orthonormal set of eigenvectors of w, β_t^i are mutually independent real

Wiener processes with incremental covariance $\lambda_i > 0$, $we_i = \lambda_i e_i$ and $trw = \sum_{i=1}^{\infty} \lambda_i$ (tr denotes the trace of an operator, see [62], [64] for more details on stochastic analysis).

We shall later consider processes $W_t = W(t, x)$ of the following form.

Proposition 4.2.1. Under the previous assumptions,

$$W_t \in \mathcal{C}([0, T]; L^2(\Omega, \mathcal{P}; H)). \tag{4.3}$$

Proof. see [10] □

4.3 Mathematical study

In this section, we investigate the well posedness of (4.1), according to C. Catté et al. [20], A. Bensoussan, R. Temam [10], E. Pardoux [62], and T.C. Garrido [36]

The variational method we will employ is defined within two fundamental spaces: a real, reflexive, and separable Banach space V, and a real Hilbert space H. We identify H with its dual and denote the dual space of V by V'. The embedding $V \hookrightarrow H$ is continuous, and V is dense in H. These relationships are summarized as:

$$V \subset H \subset V' \tag{4.4}$$

We will denote by $\|.\|$, $|\ .\ |$ and $\|.\|_*$ the norms in V, H and V' respectively; by $\langle ., . \rangle$ the duality product between V, V'.

We introduce H, V, $\mathcal{H}$ and $\mathcal{V}$ as follow

- $H = L^2(D)$, the space of square-integrable functions over D, with the inner product

$$(u, v) = \int_D u(x)v(x)dx.$$

- $V = H_0^1(D) = \left\{ v \in H, \frac{\partial v}{\partial x} \in H, \ \ with \ \ v = 0 \ \ on \, the \, boundary \, \Gamma. \right\}$
- $\mathcal{H} = L^2(\Omega \times D, \mathcal{P}; H)$, Hilbert space with scalar product

$$(u, v)_{\mathcal{H}} = E(u(.), v(.)) = \int_{\Omega} (u(w), v(w)) d\mathcal{P}(w). \tag{4.5}$$

- $\mathcal{V} = L^2(\Omega \times D, \mathcal{P}; V)$, Banach space equipped with the norm

$$\|u\|_{\mathcal{V}} = \left\{ \int_{\Omega} \|u\|_V^2 d\mathcal{P}(w) \right\}^{\frac{1}{2}}. \tag{4.6}$$

- $\mathcal{V}'$ is the dual space of $\mathcal{V}$, by the Riesz representation theorem, the norm of $A(u)$ in $\mathcal{V}'$ is

$$\|A(u)\|_{\mathcal{V}'} = \sup_{\|v\|_{\mathcal{V}} \leq 1} |\langle A(u), v \rangle|.$$

We introduce the following notation

$$A(u) = -div \left(g(|\nabla G_\sigma * u|) \nabla u \right). \tag{4.7}$$

The next lemma plays a crucial role in establishing the well-posedness of the proposed model (4.1).

Lemma 4.3.1. Let $A(.) : V \longrightarrow V'$ be a nonlinear operator defined almost everywhere in t. We assume the following hypotheses:

1. Coercivity: $\exists \nu > 0$ such that

$$\langle A(u), u \rangle_{V,V'} \geq \nu \|u\|_V^2, \qquad \forall u \in V, \quad a.e.t. \tag{4.8}$$

2. Monotonicity:

$$\langle A(u) - A(v), u - v\rangle_{V,V'} \geq 0, \qquad \forall u, v \in \mathcal{V}, \quad a.e.t. \tag{4.9}$$

3. Boundedness: $\exists \beta > 0$:

$$\|A(u)\|_{V'} \leq \beta \|u\|_V, \qquad \forall u \in V, \quad a.e.t. \tag{4.10}$$

4. Hemicontinuity:

$$\Theta \in \mathbb{R} \longrightarrow \langle A(u+\Theta v), \psi\rangle_{V,V'} \in \mathbb{R} \quad is\ continuous\ \forall u, v \in V,\ and\ \psi \in V' \quad a.e.t \in [0,T] \tag{4.11}$$

Proof. According to [20], g, G are infinitly differentiable in D. So, $g(.) \in L^\infty(0,T;\mathcal{C}^\infty(D))$. Thus, since g is decreasing, there exists a constant ν such that

$$g(|\nabla G_\sigma * \varpi|) \geq \nu \quad a.e. \in]0,T[\times D,$$

where $\|\varpi\|_{L^\infty(0,T;L^2(D))} \leq \|u_0\|_{L^2(D)}$.

1. Coersivity

$$\begin{aligned} \langle A(u), u\rangle &= -\int_D [div(g(|\nabla G_\sigma * u|)\nabla u)u]\, dx \\ &= \int_D g(|\nabla G_\sigma * u|)(\nabla u)^2 dx \\ &\geq \nu \|u\|_V^2. \end{aligned} \tag{4.12}$$

Hence, the coercivity condition hold.

2. Monotonicity

$$\begin{aligned}
\langle A(u)-A(v),u-v\rangle &= -\int_D \left[(div(g(|\nabla G_\sigma * u|)\nabla u)-div(g(|\nabla G_\sigma * v|)\nabla v))\,(u-v)\right]dx \\
&= -\int_D (div(g(|\nabla G_\sigma * u|)\nabla u)u)dx+\int_D (div(g(|\nabla G_\sigma * v|)\nabla v)u)dx \\
&\quad +\int_D (div(g(|\nabla G_\sigma * u|)\nabla u)v)dx-\int_D (div(g(|\nabla G_\sigma * u|)\nabla v)v)dx \\
&= \int_D g(|\nabla G_\sigma * u|)(\nabla u)^2dx-\int_D g(|\nabla G_\sigma * u|)\nabla u\nabla v dx \\
&\quad -\int_D g(|\nabla G_\sigma * u|\nabla u\nabla v dx+\int_D g(|\nabla G_\sigma * u|)(\nabla v)^2dx \\
&= \int_D g(|\nabla G_\sigma * u|)(\nabla u-\nabla v)^2dx \\
&\geq \nu\|u-v\|_V^2\geq 0, \qquad \forall u,v\in V. \qquad (4.13)
\end{aligned}$$

Then (4.9) hold.

3. Boundedness:

Now, we verify the boundedness condition, we use the weak form of $A(u)$ and the Cauchy-Schwartz inequality, we obtain

$$\begin{aligned}
\|A(u)\|_{V'} &= \sup_{\|v\|_V\leq 1}|\langle A(u),v\rangle| \\
&= \sup_{\|v\|_V\leq 1}|\int_D (g(|\nabla G_\sigma * u|)\nabla u\nabla v)dx| \\
&\leq \sup_{\|v\|_V\leq 1}\|g(|\nabla G_\sigma * u|)\|_{L^2(D)}\|\nabla u\|_{L^2(D)}\|\nabla v\|_{L^2(D)},
\end{aligned} \qquad (4.14)$$

by using the Poincaré inequality, we obtain

$$\|A(u)\|_{V'}\leq \beta\|u\|_V. \qquad (4.15)$$

4. Hemicontinuity

In [20], it has been shown that the operator A defined by (4.7) is weakly continuous from V to V'. Since weak continuity implies that the operator A satisfies the hemicontinuity condition. Hence, (4.11) holds. □

After proving the previous lemma, we now establish the following proposition to complete the study of the deterministic case before addressing the stochastic problem.

Proposition 4.3.2. if $u \in L^2(V)$, then

$$t \longrightarrow A(u(t)) \in L^2(V'). \tag{4.16}$$

Proof. From (4.15), we obtain

$$\|A(u(t))\|_{V'} \leq \beta\big(1 + \|u(t)\|_V\big).$$

Raising this inequality to the power $p' = \frac{p}{p-1}$ and using the elementary estimate $(a+b)^{p'} \leq 2^{p'-1}(a^{p'} + b^{p'})$ for $a, b \geq 0$, there exists a constant $C > 0$ such that, for almost every t,

$$\|A(u(t))\|_{V'}^2 \leq C\big(1 + \|u(t)\|_V^2\big).$$

Integrating over $(0, T)$ yields

$$\int_0^T \|A(u(t))\|_{V'}^2 \, dt \leq C\Big(T + \int_0^T \|u(t)\|_V^2 \, dt\Big) < \infty,$$

since $u \in L^2(0, T; V)$. This shows the integrability of $A(u(\cdot))$ in $L^2(0, T; V')$.

It remains to justify the measurability of the mapping $t \mapsto A(u(t))$ with values in V'.

The hemicontinuity assumption (4.11) ensures that, for every $v \in V$, the function

$$t \longmapsto \langle A(u(t)), v\rangle_{V',V}$$

is measurable, i.e. $A(u(\cdot))$ is weakly measurable. Since V is separable and reflexive, its dual V' is also separable; thus, by **Pettis' theorem** (see for instance [14] and [28]), weak measurability implies strong (Bochner) measurability. Hence, $A(u(\cdot)) \in L^2(0,T;V')$, then the proposition 4.3.2 hold. □

After proving lemma 4.3.1, we need to prove the following proposition 4.3.3 and lemma 4.3.4 to verify existence and uniqueness of the SPDE (4.1) in the weak sense.

Proposition 4.3.3. if $t \longrightarrow u(t)$ is a measurable mapping with values in $\mathcal{V}$, then $t \longrightarrow A(u(t))$ is measurable with values in $\mathcal{V}'$.

Proof. In our case, the operator A is independent of the variable t. According to **remark 2.1** in [10] (p. 105), the proposition 4.3.3 then holds automatically. □

Having established the properties of the operator $A : V \longrightarrow V'$ in the deterministic setting, we now extend our analysis to the stochastic framework by considering the operator $\mathcal{A} : \mathcal{V} \longrightarrow \mathcal{V}'$.

Lemma 4.3.4. the operators $\mathcal{A} : \mathcal{V} \longrightarrow \mathcal{V}'$ $t \in [0,T]$, satisfy the same properties as A

$$\text{(1)} \qquad \mathcal{A} \text{ is hemicontinuous for almost every } t, \tag{4.17}$$

$$\text{(2)} \qquad \langle \mathcal{A}(u) - \mathcal{A}(v),\, u - v\rangle_{\mathcal{V}',\mathcal{V}} \geq 0, \quad \forall\, u, v \in \mathcal{V}, \text{ for a.e. } t, \tag{4.18}$$

$$\text{(3)} \qquad \langle \mathcal{A}(u), u\rangle_{\mathcal{V}',\mathcal{V}} \geq \alpha \left\|u\right\|_{\mathcal{V}}^2, \quad \forall\, u \in \mathcal{V}, \text{ for a.e. } t, \tag{4.19}$$

$$\text{(4)} \qquad \left\|\mathcal{A}(u)\right\|_{\mathcal{V}'} \leq \beta \left\|u\right\|_{\mathcal{V}}, \quad \forall\, u \in \mathcal{V}, \text{ for a.e. } t, \tag{4.20}$$

$$\text{(5)} \qquad \text{if } u \in L^2(0,T;\mathcal{V}), \text{ then } t \mapsto \mathcal{A}(u) \in L^2(0,T;\mathcal{V}'). \tag{4.21}$$

Proof. Let u and $v \in \mathcal{V}$ and $\psi \in \mathcal{V}'$, we have, if $\Theta \in \mathbb{R}$

$$\langle \mathcal{A}(u + \Theta v), \psi(x) \rangle_{\mathcal{V},\mathcal{V}'} = \int_\Omega \langle \mathcal{A}(u(w) + \Theta v(w)), \psi(w) \rangle d\mathcal{P}(w). \tag{4.22}$$

According to 4.11, we conclude that for $\Theta \to 0$,

$$\langle \mathcal{A}(u(w) + \Theta v(w)), \psi(w) \rangle \longrightarrow \langle \mathcal{A}(u(w)), \psi(w) \rangle, \qquad \text{a.s.} \tag{4.23}$$

by using the boundedness (4.15), we obtain

$$\begin{aligned} |\langle \mathcal{A}(u(w) + \Theta v(w)), \psi(w) \rangle| &< \|\mathcal{A}(u(w)) + \Theta v(w))\|_{\mathcal{V}} \|\psi(w)\|_{\mathcal{V}} \\ &\leq \beta \|u(w) + \Theta v(w)\|_{\mathcal{V}'} \|\psi(w)\|_{\mathcal{V}} \\ &\leq \beta \left(\|u(w)\|_{\mathcal{V}'} + \|v(x)\|_{\mathcal{V}'} \right) \|\psi(w)\|_{\mathcal{V}}. \end{aligned} \tag{4.24}$$

(By limiting to $|\Theta| \leq 1$, it is sufficient).

According to Lebesgue's theorem, we obtain

$$\int_\Omega \langle \mathcal{A}(u(w) + \Theta v(w)), \psi(w) \rangle d\mathcal{P}(w) \longrightarrow \int_\Omega \langle \mathcal{A}(u(w)), \psi(w) \rangle d\mathcal{P}(w). \tag{4.25}$$

Which implies the hemicontinuous condition **(4.17)**.

To establish the condition (2), we proceed by using (4.13) and by integrating with respect to w, we obtain the monotonicity property **(4.18)**:

$$\int_\Omega \langle A(u(w)) - A(v(w)), u(w) - v(w) \rangle d\mathcal{P}(w) \geq \nu \int_\Omega \|u(w) - v(w)\|_V^2 d\mathcal{P}(w) \geq 0, \text{a.s. } w. \tag{4.26}$$

$$\langle \mathcal{A}(u) - \mathcal{A}(v), u - v \rangle_{\mathcal{V},\mathcal{V}'} \geq 0, \quad \forall\ u,\ v \quad \in \mathcal{V}. \tag{4.27}$$

Regarding **(4.19)**, we derive it from (4.12) and by integrating with respect to w, we obtain

$$\int_\Omega \langle A(u(w)), u(w)\rangle d\mathcal{P}(w) \geq \nu \int_\Omega \|u(w)\|_V^2 d\mathcal{P}(w), \qquad \forall u \in V, \quad a.s.w. \tag{4.28}$$

Which implies

$$\langle \mathcal{A}(u), u\rangle_{\mathcal{V},\mathcal{V}'} \geq \nu \|u\|_{\mathcal{V}}^2, \qquad \forall u \in \mathcal{V}. \tag{4.29}$$

Hence, the condition (3) hold. □

In the same way, **(4.20)** follows from (4.15); by integrating with respect to w, we obtain:

$$\int_\Omega \|A(u(w))\|_{V'} d\mathcal{P}(w) \leq \beta \int_\Omega \|u(w)\|_V d\mathcal{P}(w). \tag{4.30}$$

Which gives

$$\|\mathcal{A}(u)\|_{\mathcal{V}'} \leq \beta \, \|u\|_{\mathcal{V}}, \quad \forall \, u \in \mathcal{V}. \tag{4.31}$$

According to the proposition 4.3.3, $\mathcal{A}(u)$ is mesurable with values in $\mathcal{V}'$, and by (4.15), $\|A(u)\|_{V'} \leq \beta \|u\|_V$, raising this inequality to the power 2 and integrating, it follows that $\mathcal{A}(u) \in L^2(\mathcal{V}')$, this proves (4.21).

Theorem 4.3.5. Under the hypothesis of Lemma 4.3.1 and propositions 4.2.1, then there exists a unique solution $u \in L^2(\mathcal{V}) \cap \mathcal{C}(\mathcal{H})$ verifying

$$\begin{cases} \dfrac{\partial u}{\partial t} + \mathcal{A}(u) = \dfrac{\partial W}{\partial t} \quad in \;\;]0, T[\times D, \\ \qquad u(0, x) = u_0(x), \forall x \in D. \end{cases} \tag{4.32}$$

Proof. Let us consider the operator $\mathcal{A}_W : \mathcal{V} \longrightarrow \mathcal{V}'$ defined by

$$\mathcal{A}_W(v) = \mathcal{A}(v + W_t), \quad for \; v \in \mathcal{V}. \tag{4.33}$$

So, (4.32) became as follow

$$\begin{cases} \dfrac{\partial v}{\partial t} + \mathcal{A}_W(v(x)) = 0 \\ v(0,x) = u_0(x), \quad \forall x \in D. \end{cases} \tag{4.34}$$

The necessary and sufficient condition for (4.32) to have a unique solution is that (4.34) has a unique solution in $L^2(\mathcal{V}) \cap L^\infty(\mathcal{H})$, such that

$$\frac{\partial v}{\partial t} \in L^2(\mathcal{V}') + L^1(\mathcal{H})$$

Indeed, if $v \in L^2(\mathcal{V}) \cap L^\infty(\mathcal{H})$, $\dfrac{\partial v}{\partial t} \in L^2(\mathcal{V}') + L^1(\mathcal{H})$, then $v \in \mathcal{C}(\mathcal{H})$ If we set $u = v + W$, then $u \in L^2(\mathcal{V}) \cap \mathcal{C}(\mathcal{H})$ (thanks to (4.3)), and it is clear that u is a solution of (4.32).
The reverse implication shows that if u is a solution of (4.32), then $v = u - W$ is a solution of (4.34), and $\dfrac{\partial v}{\partial t} = -\mathcal{A}(u) \in L^2(\mathcal{V}')$.

Lemma 4.3.6. Let $\mathcal{A}_W : \mathcal{V} \longrightarrow \mathcal{V}'$ satisfyied

1. $\mathcal{A}_W(.)$ is hemicontinuous for a.e. t.
2. $\mathcal{A}_W(.)$ is monotone for a.e. t.
3. If $u \in L^2(\mathcal{V})$, then $\{t \longrightarrow \mathcal{A}_W(u(x)) \in L^2(\mathcal{V}')\}$.

Proof.

Let $u, v \in \mathcal{V}$ and $\psi \in \mathcal{V}'$; we have $\Theta \in \mathbb{R}$

$$\langle \mathcal{A}_W(u + \Theta v), \psi \rangle_{\mathcal{V},\mathcal{V}'} = \langle \mathcal{A}(u + W_t + \Theta v), \psi \rangle_{\mathcal{V},\mathcal{V}'}, \tag{4.35}$$

and according to (4.25), when $\Theta \longrightarrow 0$, the second member of (4.35) converges to

$$\langle \mathcal{A}(u + W_t), \psi \rangle_{\mathcal{V},\mathcal{V}'} = \langle \mathcal{A}_W(u), \psi \rangle_{\mathcal{V},\mathcal{V}'}. \tag{4.36}$$

Hence, $\mathcal{A}_W(.)$ is hemicontinuous.

To prove the monotonicity of $\mathcal{A}_W(.)$, we write

$$\langle \mathcal{A}_W(u) - \mathcal{A}_W(v), u - v \rangle = \langle \mathcal{A}(u + W_t) - \mathcal{A}(v + W_t), (u + W_t) - (v + W_t) \rangle \geq 0, \ \textit{based on } (4.9). \tag{4.37}$$

Finally, if $u \in L^2(\mathcal{V})$ and according to (4.3), then $u(.) + W(.) \in L^2(\mathcal{V})$, and therefore

$$\mathcal{A}_W u(.) = \mathcal{A}(u(.) + W(.)) \in L^2(\mathcal{V}'). \tag{4.38}$$

□

Approximation

Let N an integer intended to approach infinity and $k = \frac{T}{N}$. We consider a partition of the interval $[0, T]$, $0, k, 2k, \ldots, Nk$. We propose

$$W^n = W(nk) \in \mathcal{V}. \tag{4.39}$$

and introduce the family of operators $\mathcal{A}_W^n : \mathcal{V} \longrightarrow \mathcal{V}'$ defined by

$$\mathcal{A}_W^n \psi = \frac{1}{k} \int_{(n-1)k}^{nk} \mathcal{A}(\psi + W^n) dt. \tag{4.40}$$

Consider the recurrence relations

$$\begin{cases} \dfrac{v^n - v^{n-1}}{k} + \mathcal{A}_W v^n = 0, \\ v(0, x) = u_0 - W_0. \end{cases} \tag{4.41}$$

First, note that (4.41) uniquely defines a sequence v_n of elements in $\mathcal{V}$ (except for $n = 0$, where $v_n \in \mathcal{H}$). Indeed, introduce $\mathcal{A}^n\mathcal{V} \longrightarrow \mathcal{V}'$, defined as

$$\mathcal{A}^n\psi = \frac{1}{k}\int_{(n-1)k}^{nk} \mathcal{A}\psi dt, \quad \forall\psi \in \mathcal{V}. \tag{4.42}$$

Then (4.41) can be written as

$$\frac{v^n - v^{n-1}}{k} + \mathcal{A}^n(v^n + W^n) = 0. \tag{4.43}$$

But then, by setting $u^n = v^n + W^n$, we see that u^n must satisfy the recurrence relations

$$\begin{cases} \dfrac{u^n - u^{n-1}}{k} + \mathcal{A}^n u^n = \dfrac{W^n - W^{n-1}}{k}, \\ u^0 = u_0. \end{cases} \tag{4.44}$$

It follows from the properties of $\mathcal{A}(.)$ (Lemma 4.3.4) that $\mathcal{A}^n$ is monotone, hemicontinuous, and coercive from $\mathcal{V}$ to $\mathcal{V}'$, and consequently (cf. Lions [54]) $(I + k^n)$ is invertible. Thus, in (4.44), when u^{n-1} is known, u^n is uniquely defined as an element of $\mathcal{V}$.

We now introduce the step functions.

$$\begin{cases} W_k(t) = W^n \quad dans \quad [nk, (n+1)k[, \\ u_k(t) = u^n \quad dans \quad [nk, (n+1)k[, \\ v_k(t) = v^n \quad dans \quad [nk, (n+1)k[. \end{cases} \tag{4.45}$$

Lemma 4.3.7. $u_k(.)$ and $v_k(.)$ remain, as $k \longrightarrow 0$, within bounded subsets of $L^\infty(\mathcal{H})$ and $L^2(\mathcal{V})$.

Proof. Let us consider relation (4.43), which is written as

$$v^n - v^{n-1} + k\mathcal{A}^n u^n = 0. \tag{4.46}$$

So,

$$(v^n - v^{n-1}, v^n) + k\langle \mathcal{A}^n u^n, u^n - W^n \rangle = 0. \tag{4.47}$$

Let

$$(v^n - v^{n-1}, v^n) + k\langle \mathcal{A}^n u^n, u^n \rangle = k\langle W^n, \mathcal{A}^n u^n \rangle. \tag{4.48}$$

but

$$(v^n - v^{n-1}, v^n) = \frac{1}{2}(|v^n|^2 - |v^{n-1}|^2) + \frac{1}{2}|v^n - v^{n-1}|^2. \tag{4.49}$$

Thus (4.48) implies

$$|v^n|^2 - |v^{n-1}|^2 + |v^n - v^{n-1}|^2 + 2k\langle \mathcal{A}^n u^n, u^n \rangle = 2k\langle W^n, \mathcal{A}^n u^n \rangle. \tag{4.50}$$

According to properties (4.19) and (4.20) of $\mathcal{A}$, which lead to the same for $\mathcal{A}^n$, we deduce from (4.50) the following estimate

$$|v^n|^2 - |v^{n-1}|^2 + 2k\nu\|u^n\|^2 \leq 2k\beta\|W^n\|_{\mathcal{V}}\|u^n\|_{\mathcal{V}}. \tag{4.51}$$

We then use the following classic inequality: if $i, j > 0$ satisfy $1/i + 1/j = 1$, then

$$ab \leq \frac{a^i c^i}{i} + \frac{b^j}{jc^j}, \quad \forall a, b, c > 0.$$

Therefore, we have

$$\|W^n\|_{\mathcal{V}}\|u^n\|_{\mathcal{V}}^{p-1} \leq \|u^n\|_{\mathcal{V}}^p \frac{l^{p'}}{p'} + \|W^n\|_{\mathcal{V}}^p \frac{1}{pl^p}, \quad \forall l > 0. \tag{4.52}$$

Let us choose l such that $C = 2\nu + 2\beta\dfrac{l^2}{2}$. Then, taking into account (4.52), we deduce from

(4.51) the following inequality

$$|v^n|^2 - |v^{n-1}|^2 + kC\|u^n\|^2 \leq \frac{2k\beta}{2l^2}\|W^n\|_{\mathcal{V}}. \tag{4.53}$$

Since $W_t \in \mathcal{C}(\mathcal{V})$,

$$\|W^n\|_{\mathcal{V}} \leq C_1, \quad \forall n. \tag{4.54}$$

Thanks to (4.54), we finally obtain the upper bound

$$|v^n|^2_{\mathcal{H}} - |v^{n-1}|^2_{\mathcal{H}} + kC\|u^n\|^2_{\mathcal{V}} \leq kC_2. \tag{4.55}$$

Where $C_2 = 2C_1\dfrac{\beta}{2l^2}$.

By summing, we easily deduce the following bounds from (4.55).

$$\begin{cases} \forall n, |v^n|^2_{\mathcal{H}} \leq |u_0 - W_0|^2_{\mathcal{H}} + TC_2, \\ C\sum_{n=1}^{N} k\|u^n\|^2_{\mathcal{V}} \leq |u_0 - W_0|^2_{\mathcal{H}} + TC_2, \end{cases} \tag{4.56}$$

but (4.56) means that u_k remains bounded in $L^2(\mathcal{V})$ and v_k remains bounded in $L^\infty(\mathcal{H})$. Since W_k remains bounded in $L(\mathcal{V})$, the lemma follows.

Let t be a fixed value in $[0, T]$, and define $n_t = \frac{t}{k}$. By summing the discrete relations for n from 1 to n_t, we obtain

$$v^{n_t} + k\sum_{n=1}^{n_t} \mathcal{A}^n u^n = u_0 - W_0, \tag{4.57}$$

which is also written as

$$v_k(t) + \int_0^{n_t k} \mathcal{A}_k u_k(s)ds = u_0 - W_0. \tag{4.58}$$

Also, $\mathcal{A}_k$ can be replaced by $\mathcal{A}$ in this equality (see [10]). Now, let $\chi \in \mathcal{V}$, (4.58) gives the following

$$(v_k(t), \chi) + \int_0^T \langle \mathcal{A}u_k(s), \zeta_{n_t k}(s)\chi\rangle ds = u_0. \tag{4.59}$$

Where $\zeta_{n_t k}(s)$ denotes the characteristic function of $]0, n_t k[$.

Lemma (4.3.7) allows us to extract sequences u_k and $v_k(t)$ from subsequences denoted in the same way, which converge to elements u and v in weak $L^2(\mathcal{V})$ and weak-star $L^\infty(\mathcal{H})$. It is evident that $u = v + W$. Furthermore, according to property (4.20) of $\mathcal{A}$, we deduce from Lemma (4.3.7) that $\mathcal{A}u_k(s)$ remains bounded in $L^2(\mathcal{V}')$ and, by extracting a new subsequence if necessary, we can always assume that $\mathcal{A}u_k(.) \longrightarrow \Psi(s)$ weakly in $L^2(\mathcal{V}')$. We can then take the limit in (4.59) and obtain

$$(v_k(t), \chi) + \int_0^t \langle \Psi(s), \chi \rangle ds = u_0. \tag{4.60}$$

Then

$$\frac{dv}{dt} + \Psi(t) = 0, \quad a.e.\ t \in [0, T]\ \ (equality\ \ in\ \ \mathcal{V}'). \tag{4.61}$$

□

Then we have the following lemma.

Lemma 4.3.8.

$$\Psi(t) = \mathcal{A}u(t), \quad a.e.\ t \in [0, T]. \tag{4.62}$$

Proof. First, let's prove that

$$\int_0^T \langle \mathcal{A}u_k(s), u_k(s) \rangle ds \xrightarrow{k \longrightarrow 0} \int_0^T \langle \Psi(s), u(s) \rangle ds. \tag{4.63}$$

Indeed, (4.61) shows that $\dfrac{dv}{dt} \in L^2(\mathcal{V}')$. Since $v \in L^2(\mathcal{V})$, it follows (cf. [54]) that we have

$$\frac{d}{dt}|v(t)|^2_{\mathcal{H}} = 2\langle v(t), \frac{dv}{dt}(t) \rangle_{\mathcal{V}, \mathcal{V}'} \quad a.e.\ t. \tag{4.64}$$

Let

$$|v(T)|^2 = |v(0)|^2 + 2\int_0^T \langle v(t), -\Psi(t)\rangle_{\mathcal{V},\mathcal{V}'} dt. \tag{4.65}$$

Next, consider the equalities (4.50), which we sum over n from 1 to N. From this, we easily deduce the inequality

$$|v_k(T)|^2 + 2\int_0^T \langle \mathcal{A}u_k, u_k(t)\rangle dt \leq |v(0)| + 2\int_0^T \langle W_k(t), \mathcal{A}u_k(t)\rangle. \tag{4.66}$$

By taking the upper limit, we obtain

$$\limsup_{k\longrightarrow 0} \int_0^T \langle \mathcal{A}u_k(t), u_k(t)\rangle dt \leq \frac{1}{2}|v(0)|^2 + \int_0^T \langle W_k(t), \Psi(t)\rangle - \liminf_{k\longrightarrow 0} \frac{1}{2}|v_k(T)|^2, \tag{4.67}$$

but,

$$\frac{1}{2}|v(T)|^2 \leq \liminf_{k\longrightarrow 0} \frac{1}{2}|v_k(T)|^2,$$

and considering (4.65), we then deduce from (4.67)

$$\begin{aligned} \limsup_{k\longrightarrow 0} \int_0^T \langle \mathcal{A}u_k(t), u_k(t)\rangle dt &\leq \frac{1}{2}|v(0)|^2 + \int_0^T \langle W_k(t), \Psi(t)\rangle - \frac{1}{2}|v(0)|^2 - \int_0^T \langle u(t) - W_t, -\Psi(t)\rangle dt \\ &= \int_0^T \langle u(t), \Psi(t)\rangle dt, \end{aligned} \tag{4.68}$$

and as $\mathcal{A}$ is monotone, we deduce that

$$\liminf_{k\longrightarrow 0} \int_0^T \langle \mathcal{A}u_k(t), u_k(t)\rangle dt \geq \int_0^T \langle \Psi(t), u(t)\rangle dt, \tag{4.69}$$

which, compared with (4.68), clearly shows (4.63).

To prove Lemma (4.3.8) from (4.63), we use a classical technique based on the monotonicity and hemicontinuity of $\mathcal{A}$ (cf. Minty [57], Brézis [13], and Lions [54]).

According to the monotonicity of $\mathcal{A}$, we have, for all $\phi \in L^2(\mathcal{V})$

$$\int_0^T \langle \mathcal{A}u_k(t) - \mathcal{A}\phi(t), u_k(t) - \phi(t)\rangle dt \geq 0. \tag{4.70}$$

Thus, by passing to the limit, thanks to (4.63), it follows that

$$\int_0^T \langle \Psi(t) - \mathcal{A}\phi(t), u(t) - \phi(t)\rangle dt \geq 0. \tag{4.71}$$

We then choose, $\phi(t) = u(t) - \gamma\varphi(t)$, where $\varphi \in L^2(\mathcal{V})$ and $\gamma > 0$ are arbitrary; (4.71) became as follow

$$\int_0^T \langle \Psi(t) - \mathcal{A}(u(t) - \gamma\varphi(t)), \gamma\varphi(t)\rangle dt \geq 0, \tag{4.72}$$

we devise then by γ, we obtain

$$\int_0^T \langle \Psi(t) - \mathcal{A}(u(t) - \gamma\varphi(t)), \varphi(t)\rangle dt \geq 0. \tag{4.73}$$

We then let γ tend to 0 in (4.73). The property of hemicontinuity leads to

$$\int_0^T \langle \Psi(t) - \mathcal{A}u(t), \varphi(t)\rangle dt \geq 0. \tag{4.74}$$

So, the result holds. □

Prove of the theorem 4.3.5

We summarize the results obtained. There exists $v \in L^2(\mathcal{V})$, $\dfrac{dv}{dt} \in L^2(\mathcal{V}')$ and $u \in L^2(\mathcal{V})$ such that $u = v + W$. Moreover (4.61) and the Lemma 4.3.8 give

$$\frac{dv}{dt} + \mathcal{A}u(t) = 0. \tag{4.75}$$

Finally, $v(0) = u(0) - W_0$ (according to (4.60)). Then v is a solution of (4.34), and consequently u of (4.32)

Uniqueness follows from the monotonicity property of the operator $\mathcal{A}_{W_t}$. Indeed, Suppose that (4.34) has two solutions v_1, v_2, and let $\chi = v_1 - v_2$. . We then have, by subtraction,

$$\begin{cases} \dfrac{d\chi}{dt} + \mathcal{A}_W v_1 - \mathcal{A}_W v_2 = 0 \quad a.e. \quad t, \\ \chi(0) = 0. \end{cases} \tag{4.76}$$

And thus, by multiplying by χ and integrating, we get

$$\frac{1}{2}|\chi(t)|^2 + \int_0^t \langle \mathcal{A}_{W_s} v_1(s) - \mathcal{A}_{W_s} v_2(s), v_1(s) - v_2(s)\rangle ds = 0, \quad \forall t \in [0,T], \tag{4.77}$$

and since $\mathcal{A}_{W_t}$ is monotone, we see that $\chi(t) = 0$, $\forall t$.

4.4 Energy estimates and stability analysis

This section establishes energy estimates to verify the stability of solutions. We will need to consider process of the form W, which satisfy condition (4.3). As for the correlations between W, u, we will assume the following hypothesis.

Hypothesis

$\forall t_1, t_2$ with $0 \leq t_1 \leq t_2 \leq T$, $W_{t_1} - W_{t_2}$ is a random variable taking values in H independent of the random variable $\{u_0, W(t_{j_1}), ..., W(t_{j_q}))\}$ taking values in $H \times H^q$ $\forall q$ and $t_{j_1}, ..., t_{j_q} \leq t_1$.

Based on the previously stated hypotheses, we derive the following theorem.

Theorem 4.4.1. Under the assumptions stated in Lemma (4.3.6) and hypothesis above, the following energy equality hold

$$E\|u(t)\|_H^2 + 2E\int_0^t \langle A(s)u(s), u(s)\rangle ds = E\|u(0)\|_H^2 + E\|W(t)\|_H^2 \quad \forall t \in [0,T]. \tag{4.78}$$

Proof. See [10] □

Now, we prove the following stability result.

Proposition 4.4.2. Consider $W \in \mathcal{C}([0,T]; L^2(D,\mathcal{P};H))$, $u_0 \in H_0^1(D)$ and u associated solution, then for any t,

$$E\|u(t)\|_H^2 \leq E\|u(0)\|_H^2 + E\|W(t)\|_H^2 \quad \forall t \in [0,T]. \tag{4.79}$$

Proof. Since the operator A(t) verify the coersivity condition, meaning $\langle A(t)u(t), u(t)\rangle \geq \nu\|u(t)\|^2$, the energy equality (4.78) became as follow

$$E\|u(t)\|_H^2 + 2\nu E\int_0^t \|u(s)\|^2 ds \leq E\|u(0)\|_H^2 + E\|W(t)\|_H^2, \tag{4.80}$$

we know $2\nu E\int_0^t \|u(s)\|^2 ds \geq 0$, we substitute that in (4.80), we obtain

$$E\|u(t)\|_H^2 \leq E\|u(0)\|_H^2 + E\|W(t)\|_H^2, \quad \forall t \in [0,T]. \tag{4.81}$$

Hence, the proposition **4.4.2** hold. □

4.5 Numerical discretisation

The SPDE-based denoising scheme is approximated by applying a finite-difference based method. Thus, we put a space grid size of $\Delta x = \Delta y = 1$ and a time step $\Delta t = \frac{T}{N}$, where T and N are the final time and the number of iterations respectively.

$$\begin{aligned} u_{i,j}^{n+1} &= u_{i,j}^{n} + \Delta t \left[g_{i,j}^{n} \left(u_{i+1,j}^{n} + u_{i-1,j}^{n} + u_{i,j+1}^{n} + u_{i,j-1}^{n} - 4u_{i,j}^{n} \right) \right] \\ &\quad + \frac{\Delta t}{4} \left[(g_{i+1,j}^{n} - g_{i-1,j}^{n})(u_{i+1,j}^{n} - u_{i-1,j}^{n}) \right] \\ &\quad + \frac{\Delta t}{4} \left[(g_{i,j+1}^{n} - g_{i,j-1}^{n})(u_{i,j+1}^{n} - u_{i,j-1}^{n}) + (W_{i,j}^{n+1} - W_{i,j}^{n}) \right]. \end{aligned} \tag{4.82}$$

Iterative algorithm given by (4.82), it begins by inputting the initial conditions which is the noisy image u^0, and the continuous Wiener process W_t, a.e.t. Then, we repeat N+1 times by using the numerical scheme (4.82). Finally, we get the restored image u^{N+1} without noise.

4.5.1 Stability analysis

In this section, we study the stability of the numerical scheme using the Fourier transform method. Specifically, we implement this change in (4.82), given by:

$$u_{i,j}^{n} = \hat{u}^{n} e^{I\pi(ki+mj)}. \tag{4.83}$$

Definition 4.1. Scheme (4.82) said to be stable, if there exists a constant C such that

$$\left| \frac{\hat{u}^{n+1}}{\hat{u}^{n}} \right| \leq C\Delta t. \tag{4.84}$$

let us find the stability condition for (4.82), i.e find the constant C in (4.84)

Proposition 4.5.1. If (4.2) satisfied g, then

$$\Delta t \leq \frac{2}{8 - \xi_n}, \quad \xi_n = W_{i,j}^{n+1} - W_{i,j}^{n}. \tag{4.85}$$

Proof. We substitute (4.83) in (4.82) as follow

$$\begin{aligned}
\hat{u}^{n+1}e^{I\pi(ki+mj)} &= \hat{u}^n e^{I\pi(ki+mj)} + \Delta t g^n_{i,j}\left(\hat{u}^n e^{I\pi(k(i+1)+mj)} + \hat{u}^n e^{I\pi(k(i-1)+mj)}\right) \\
&+\Delta t g^n_{i,j}\left(\hat{u}^n e^{I\pi(ki+m(j+1))} + \hat{u}^n e^{I\pi(ki+m(j-1))} - 4\hat{u}^n e^{I\pi(ki+mj)}\right) \\
&+\frac{\Delta t}{4}\left[(g^n_{i+1,j} - g^n_{i-1,j})(\hat{u}^n e^{I\pi(k(i+1)+mj)} - \hat{u}^n e^{I\pi(k(i-1)+mj)})\right] \\
&+\frac{\Delta t}{4}(g^n_{i,j+1} - g^n_{i,j-1})(\hat{u}^n e^{I\pi(ki+m(j+1)} - \hat{u}^n e^{I\pi(ki+m(j-1))}) \\
&+\Delta t(W^{n+1}_{i,j} - W^n_{i,j}),
\end{aligned}$$

$$\begin{aligned}
\hat{u}^{n+1}e^{I\pi(ki+mj)} &= \hat{u}^n e^{I\pi(ki+mj)}\left(1 + \Delta t\left(g^n_{i,j}\left(e^{I\pi k} + e^{-I\pi k} + e^{I\pi m} + e^{-I\pi m} - 4\right)\right)\right) \\
&+\hat{u}^n e^{I\pi(ki+mj)}\left(\frac{\Delta t}{4}(g^n_{i+1,j} - g^n_{i-1,j})(e^{I\pi k} - e^{-I\pi k})\right) \\
&+\hat{u}^n e^{I\pi(ki+mj)}\left(\frac{\Delta t}{4}(g^n_{i,j+1} - g^n_{i,j-1})(e^{I\pi m} - e^{-I\pi m})\right) \\
&+\Delta t(W^{n+1}_{i,j} - W^n_{i,j}),
\end{aligned}$$

$$\begin{aligned}
\frac{\hat{u}^{n+1}e^{I\pi(ki+mj)}}{\hat{u}^n e^{I\pi(ki+mj)}} &= 1 + \Delta t\left(g^n_{i,j}\left(e^{I\pi k} + e^{-I\pi k} + e^{I\pi m} + e^{-I\pi m} - 4\right)\right) \\
&+\frac{\Delta t}{4}(g^n_{i+1,j} - g^n_{i-1,j})(e^{I\pi k} - e^{-I\pi k}) \\
&+\frac{\Delta t}{4}(g^n_{i,j+1} - g^n_{i,j-1})(e^{I\pi m} - e^{-I\pi m}) \\
&+\Delta t\left(\frac{W^{n+1}_{i,j} - W^n_{i,j}}{\hat{u}^n e^{I\pi(ki+mj)}}\right).
\end{aligned}$$

Such as $g^n_{i,j} \leqslant 1$, $g^n_{i+1,j} \leqslant 1$, $g^n_{i-1,j} \leqslant 1$, $g^n_{i,j+1} \leqslant 1$ and $g^n_{i,j-1} \leqslant 1$

and

$$\begin{cases}
e^{I\pi k} + e^{-I\pi k} = 2cos(\pi k), \\
e^{I\pi m} + e^{-I\pi m} = 2cos(\pi m),
\end{cases} \tag{4.86}$$

$$\Rightarrow \begin{cases} 2cos(\pi k) - 2 = -4sin^2\left(\dfrac{\pi k}{2}\right), \\ 2cos(\pi m) - 2 = -4sin^2\left(\dfrac{\pi m}{2}\right). \end{cases} \tag{4.87}$$

With $sin^2\left(\dfrac{\pi k}{2}\right) \leq 1$, $sin^2\left(\dfrac{\pi m}{2}\right) \leq 1$,

$$\begin{aligned} \left|\frac{\hat{u}^{n+1}}{\hat{u}^n}\right| &\leq \left|1 - 8\Delta t + \Delta t\left(\frac{W_{i,j}^{n+1} - W_{i,j}^n}{\hat{u}^n e^{I\pi(ki+mj)}}\right)\right| \\ &\leq \left|1 - 8\Delta t + \Delta t(W_{i,j}^{n+1} - W_{i,j}^n)\right| \\ &\leq |1 - \Delta t\,(8 - \xi_n)| \end{aligned}$$

$$\begin{aligned} |1 - \Delta t\,(8 - \xi_n)| \leq 1 \quad &\Rightarrow \quad -1 \leq \Delta t\,(8 - \xi_n) \leq 1 \\ &\Rightarrow \quad \Delta t \leq \frac{2}{8 - \xi_n}. \end{aligned} \tag{4.88}$$

Then the proposition **4.5.1** hold.

if we considered

$$\Delta t \leq \frac{2}{8 - \xi_n} = \frac{1}{4 - \frac{1}{2}\xi_n} = \frac{1}{C}. \quad C = 4 - \frac{1}{2}\xi_n. \tag{4.89}$$

This gives stability conditions (4.89) for a good choice of the time discretisation parameter to solve (4.82). □

4.5.2 Numerical results and comments

In this section, we present the results of our numerical experiments using MATLAB R2022b. We tested different approaches to evaluate the performance of our SPDE model for image restoration. To measure the quality of the restored images, we calculated the Peak Signal-to-Noise Ratio (**PSNR**) and the Structural Similarity Index (**SSIM**). The experiments consider both Gaussian and salt & pepper noise conditions.

Models	PDE Barbu	SDE Barbu	Borkowski	PM1	PM2	SPDE 1	SPDE 2
$\gamma = 0.1$	21.3094	20.1880	24.6288	24.1495	24.1601	**27.6852**	**27.6852**
$\gamma = 0.01$	24.3094	30.1259	30.0948	30.2702	30.1051	**33.3760**	**33.3760**

Table 4.1: **PSNR** values for denoised images with Gaussian Noise

Models	PDE Barbu	SDE Barbu	Borkowski	PM1	PM2	SPDE 1	SPDE 2
$\gamma = 0.1$	0.6008	0.5391	0.6104	0.6769	0.6766	**0.7559**	**0.7559**
$\gamma = 0.01$	0.6017	0.7111	0.8160	0.8035	0.8040	**0.8913**	**0.8913**

Table 4.2: **SSIM** Values for Denoised Images with Gaussian Noise

We put our SPDE model to the test by varying the standard deviation (σ) of the Gaussian filter, while keeping the noise variance fixed at $\gamma = 0.1$ & 0.01. This allowed us to evaluate how well the model adapts to different smoothing conditions in image denoising. The results, presented in table 4.3.

σ	0.45		0.9		1		1.6	
γ	0.1	0.01	0.1	0.01	0.1	0.01	0.1	0.01
PSNR	22.7798	33.5837	25.2683	26.6396	25.1102	27.9571	24.6648	26.2707
SSIM	0.55131	0.8915	0.7466	0.8404	0.7153	0.8381	0.7104	0.8188

Table 4.3: Impact of Gaussian Filter Variance on Image Quality Metrics (PSNR & SSIM) Under Fixed Noise Level $\gamma = 0.1$ & 0.01

Model	PDE Barbu	SDE Barbu	SDE Borkowski	PM 1	PM 2	SPDE 1	SPDE 2
PSNR	22.9429	**34.3444**	30.9117	31.6016	32.2173	**35.4783**	**35.4783**
SSIM	0.7748	**0.9739**	0.8999	0.9613	0.9642	**0.9861**	**0.9861**

Table 4.4: Performance of Our **SPDE** Model with Salt-and-Pepper Noise Compared to Other Approaches Under a Fixed Noise Level $\gamma = 0.1$ and $\sigma = 0.45$

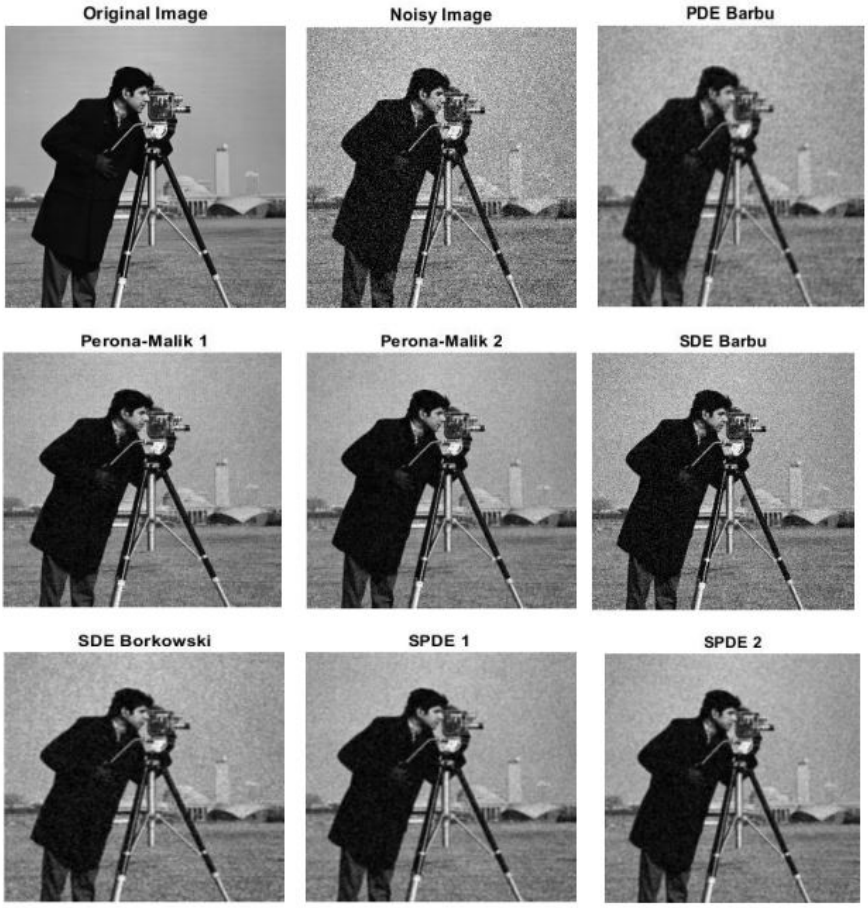

Figure 4.1: Restored image by using different approaches with $\mathbf{\Delta t} = T/N$, $\mathbf{N = 100}, \mathbf{T = 1}$, $\gamma = 0.1$.

We denote:

- **PDE Barbu**: the Klomogorov PDE related to SDE of Barbu [5].
- **SDE Barbu**: the model introduced by Barbu in 2016 [5].
- **Perona-Malik 1** and **Perona-Malik 2**: the model of **PM** [63] with their decreasing functions (4.2) (fractional and exponontial respectively).
- **SDE Borkowski**: Borkowski's model, introduced in 2013 [15]
- **SPDE 1** and **SPDE 2**: the used of exponential and fractional functions (4.2) respectively

Figure 4.2: Restored image results after 'salt & Pepper' noise application with $\mathbf{\Delta t} = T/N$, $\mathbf{N = 5, T = 1}$, $\gamma = 0.1$ and $\sigma = 0.45$

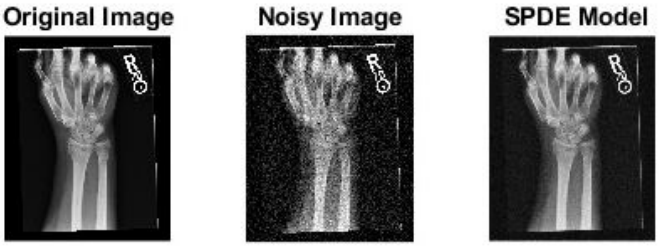

Figure 4.3: Restored image result after 'Gaussian noise' application with $\mathbf{\Delta t} = T/N$, $\mathbf{N = 5, T = 1}$, $\gamma = 0.1$ and $\sigma = 0.45$

Comments On Numerical Results

By closely observing **Table 4.1, 4.2, 4.3, and 4.4** as well as **Figure 4.1**, **4.2** and **4.3**, we notice that

- The restoration performance under Gaussian noise varied across models. As shown in Tables 4.1, 4.2, the Barbu (SDE and PDE) models exhibited inferior performance compared to the PM 1, PM 2, and SDE Borkowski models, as reflected in their PSNR and SSIM values. Specifically, with $\gamma = 0.1$ the Barbu SDE model achieved a PSNR of 20.1880 dB and an SSIM of 0.5391, which is lower than the PM 1 (PSNR:24.1495 dB, SSIM:0.6769) and PM 2 (PSNR:24.1601 dB, SSIM:0.6766) models. This discrepancy underscores the critical role of diffusion in image restoration—an aspect Barbu's model neglects by relying solely on the drift term. In contrast, our proposed model, which integrates both EDS and EDP, achieves superior restoration quality, surpassing models that employ either EDS or EDP alone. As indicated by the PSNR of 27.6852 dB and SSIM of 0.7559 in our approach, these findings confirm its effectiveness and further highlight the advantage of SPDE in enhancing image restoration.

- Our proposed model incorporates regularization through the convolution of the functions g and G_{sigma}, which plays a crucial role in enhancing image quality while preserving fine details. The precise selection of the parameter σ is essential for obtaining optimal restoration results, as demonstrated by the quantitative evaluations in Table

4.3. Specifically, selecting $\sigma = 0.9$ with $\gamma = 0.1$ led to an increase in PSNR to 25.2683 dB and SSIM to 0.7466, and $\sigma = 0.45$ with $\gamma = 0.01$ led to an increase in PSNR to 33.5837 dB and SSIM to 0.8915, reinforcing the importance of careful parameter tuning in achieving superior denoising performance.

- For salt-and-pepper noise, all models demonstrated notable performance improvements, achieving higher PSNR and SSIM values. However, while the Barbu SDE model performed significantly better under salt & pepper noise than under Gaussian noise, it was still outperformed by our proposed approach. As shown in Table 4.4, the Barbu SDE model achieved a PSNR of 34.3444 dB and an SSIM of 0.9739, whereas our method attained the highest values, with a PSNR of 35.4783 dB and an SSIM of 0.9861 These results confirm the effectiveness of our approach in reducing noise while preserving image structure and fine details. Additionally, the visual assessment in Figure 2 further supports these findings, where our approach produced sharper and more natural restorations compared to competing models.

4.6 Conclusion

In this work, we introduced an effective image restoration technique based on Stochastic Partial Differential Equations (SPDEs), integrating the Perona-Malik (PM) equation with stochastic perturbations for enhanced noise removal while preserving fine details. We also conducted a comprehensive mathematical study of the model, analyzing both its theoretical and numerical stability, which confirmed its robustness under various conditions.

The results, supported by the PSNR and SSIM values of 33.3760 and 0.8293, demonstrate superior performance in noise reduction and structural integrity compared to other methods. These findings highlight the potential of our SPDE-based model for high-quality image restoration.

Chapter 5

General conclusion and perspectives

Throughout this work, we have undertaken an in-depth study of image restoration through stochastic differential equations (SDEs) and stochastic partial differential equations (SPDEs). Our research involved not only the theoretical analysis of these models but also their numerical implementation and evaluation (see [40]). This dual approach allowed us to better understand the local geometric behavior of existing restoration methods and guided us toward the design of more efficient models.

In the first part of the thesis, we introduced the mathematical foundations necessary for our study, including functional spaces, the stochastic framework, and numerical methods such as finite differences and the Euler–Maruyama scheme. Building upon these preliminaries, we were able to analyze classical PDE-based models and evaluate their capabilities and limitations in handling noise and degradation.

In the second part, we proposed an original contribution by extending the classical Perona–Malik model into a stochastic framework. To this end, we carefully designed drift and diffusion terms inspired by Barbu and Borkowski, while incorporating stochastic perturbations to better capture uncertainties in image data. We rigorously established the well-posedness of this model using Øksendal's theorem and analyzed its stability through Fourier

techniques. On the numerical side, the Euler–Maruyama scheme combined with Monte Carlo simulations enabled us to approximate solutions effectively. The experimental results confirmed the efficiency of our approach, showing competitive performance in terms of PSNR, SSIM, and visual quality when compared with existing algorithms [4], [5], [16] and [17].

The last chapter extended our study to stochastic partial differential equations (SPDEs), which generalize the SDE framework to continuous spatial domains. This extension allowed us to model the evolution of image intensity as a random field, thus capturing both spatial and temporal uncertainties. We analyzed the existence and uniqueness of weak solutions for the proposed SPDE using variational methods and stochastic analysis tools. The model demonstrated strong potential for improving image restoration, especially in highly noisy or uncertain environments, while maintaining mathematical rigor and numerical stability.

Perspectives.

Several promising research directions emerge from this work. A natural extension involves the development of three-dimensional stochastic models dedicated to medical image restoration, particularly for MRI or CT volumetric data. Such 3D models would make it possible to exploit spatial correlations across slices, improving both the consistency and accuracy of the reconstructed structures. Another potential direction concerns the application of the proposed stochastic framework to image inpainting problems, where missing or damaged regions must be reconstructed. Integrating stochastic diffusion with geometry-aware priors could enhance the preservation of edges and textures during inpainting. Finally, future work could focus on adaptive or learning-based drift and diffusion terms, aiming to develop hybrid models that are both mathematically sound and highly effective in practice.

Bibliography

[1] K. B. Athreya and S.N. Lahiri, Measure Theory and Probability Theory, Springer, 2006.

[2] G. Aubert and P. Kornprobst, Mathematical Problems in Image Processing, Partial Differential Equations and the Calculus of Variations (second edition) Applied Mathematical Sciences, Springer-Verlag, 2006.

[3] I. Avcibas, B. Sankur and K. Sayood, Statistical evaluation of image quality measures, Journal of Electronic Imaging, vol. 11, no. 2, pp. 206-223, 2002.

[4] T. Barbu, G. Da Prato and L. Tubaro, Kolmogorov equation associated to the stochastic reflection problem on a smooth convex set of a Hilbert space II, Annales de l'IHP Probabilités et Statistiques, 699-724, 2011.

[5] T. Barbu, et A. Favini, Novel stochastic differential model for image restoration. Processings of the Romanian Academy-Series A: Mathematics, Physics, Technical Sciences, Information Science. vol. 17, no. 2, pp. 109-116, 2016.

[6] C. Bauzet, J. Jiacomoni, G. Vallet, On a Class of Quasilinear Barenblatt Equation, Monografias de la Real Academia de Ciencias de Zaragoza 38: p. 35-51, 2012.

[7] C. Bauzet, Étude d'équations aux dérivées partielles stochastiques, Hal Open Science, 2013.

[8] A. Ben Hamza and H. krim A Variational Approach to Maximum a Posteriori Estimation for Image Denoising, Energy Minimization Methods in Computer Vision and Pattern Recognition, 19-34, 2001.

[9] M. Benseghir, F.Z. Nouri, A new partial differential equation for image inpainting, Bol. Soc. Paran. Mat. 137-155, 2021.

[10] A. Bensoussan and R. Temam, Equations aux dérivées partielles stochastiques non lineaires(1), 1971.

[11] A. Belahmidi , Equations aux dérivées parielles appliquées à la restauration et a l'agrandissement des images, Thèse de doctorat, Université Paris IX-Dauphine, 2003.

[12] M. Black, G. Sapiro, D. Marimont, D. Heeger, Robust anisotropic diffusion", IEEE Transactions on Image Processing, vol.7, no.3, pp. 421-432, 1998.

[13] H. Brézis and M. Sibony, Méthodes d'Approximation et d'Itération pour les Opérateurs Monotones, Mémoire présenté par J.L. Lions, 1971.

[14] H. Brézis, Functional Analysis, Sobolev Spaces and Partial Differential Equations, Springer, 2011.

[15] D. Borkowski, K.J. Borkowska, Image restoration using anisotopic stochastic diffusion collaborated with non local means, In IFIP Internatinal Conference on Computer Information Systems and Industial Management, Krakow, Poland, 177-189, 2013.

[16] D. Borkowski, Forward and backward filtering based on backward stochastic differential equations, Inverse Problems and Imaging, 305-325, 2016.

[17] D. Borkowski and K.J. Borkowska, Image denoising using backward stochastic differential equations, Advances in Intelligent Systems and Computing, 185-194, 2017.

[18] M. Borroto-Fernández, M. González-Hidalgo, and A. León-Mecı'as, New estimation method of the contrast parameter for the Perona-Malik diffusion equation, Computer Methods In Biomechanics And Biomedical Engineering: Imaging and Visualization, Vol. 4 , No. 3-4, pp. 238-252, 2016.

[19] A. Buades, B. Coll and J. M. Morel, n-Local Means Denoising, Image Processing On Line, 1, pp. 208–212, https://doi.org/10.5201/ipol.2011.bcm nlm, 2011.

[20] C. Catté, P.L. Lions, J.M. Morel and T. Coll, Image Selective Smoothing and Edge Detection by Nonlinear Diffusion, SIAM J. NUMER. ANAL, vol.29, No. 1, pp.182-193, 1992.

[21] T. Chan, A. Marquina, and P. Mulet, High-Order Total Variation-Based Image Restoration, SIAM Journal on Scientific Computing, Vol. 22, 2000.

[22] P. Charbonnier, L. Blanc-Fèraud, G. Aubert, and M. Barlaud. Deterministic edge-preserving regularization in computed imaging. IEEE Transactions on Image Processing, 6(2):298-311, February 1997.

[23] G. Da Prato and J. Zabczyk, Stochastic equations in infinite dimensions, Cambridge University Press, Series Encyclopedia of Mathematics and its Applications, 44, 1992.

[24] M. Dassa, Equations de Kolmogorov et EDP, Master en Mathématiques, 2019.

[25] X. Descombes and E. Zhizhina, 'Image Denoising using Stochastic Differential Equations', INRIA, 2003.

[26] X. Descombes, E. Zhizhina, Image denoising using stochastic differential equations, Rappord de recherche, HAL Open Science, 2006.

[27] X. Descombes,M. Lebellego and E. Zhizhina, Image deconvolution using a stochastic differential equation approach, In Proceedings of The Second International on Computer Vision Theory and Applications, 157-164, 2007.

[28] J. Diestel and J. J. Uhl, Vector Measures, Mathematical Surveys and Monographs, American Mathematical Society, 1977.

[29] M. Diwakar and M. Kumar, A review on CT image noise and its denoising, ELSEVIER, Biomedical Signal Processing and Control, 73-88, 2018.

[30] R. Dosselmann and X.-D. Yang, Existing and emerging image quality metrics. In Canadian Conference on Electrical and Computer Engineering, pp. 1906-1913, 2005.

[31] J. Dulauroy, Formule de Feynman-Kac et Equation de Black et Scholes: relations entre EDP et EDS, Université Paul Verlaine de Metz UFR de Mathématiques, 2010.

[32] B. Ewald, M. Petcu and R. Temam, 'Stochastic Solutions of the two dimensional primitive equations of the ocean and atmosphere with an additive noise, Anal. Appl. (Singap) 5(2), p.183-198, 2007.

[33] L. Fan, F. Zhang, H. Fan and C. Zhang, Brief review of image denoising techniques, Visual Computing for Industry, Biomedicine, and Art, Springer Open, 1-12, 2019.

[34] M. A. T. Figueiredo, Bayesian Methods and Markov Random Fields, CVPR-98, Santa Barbara, CA, USA.

[35] L. Florack. Image Structure. Kluwer Academic Publishers, 1997.

[36] T.C. Garrido, 'Existence and Uniqueness of Solutions for Non-Linear Stochastic Partial Differential Equations', Departamento de Anàlisis Matemàtico, Universidad de Sevilla, Apartado de Correos 1.160. 41080-SEVILLA, Spain.

[37] P. Getreuer, Rudin–Osher–Fatemi Total Variation Denoising using Split Bregman, Image Processing On Line, 2, pp. 74–95, 2012. https://doi.org/10.5201/ipol.2012.g-tvd

[38] G. Gilboa, N. Sochen, Y. Zeevi - Forward-and-backward diffusion processes for adaptive image enhancement and denoising, IEEE Transactions on Image Processing, vol.11, no.7, pp.689-703, 2002.

[39] R. C. Gonzalez and R. E. Woods, Digital Image Processing Third Edition, Pearson International Edition, 2008.

[40] R. Halilou, F. Z. Nouri and M. L. Hadji, A New Stochastic Partial Differential Model for Image Restoration, Communications on Applied Nonlinear Analysis, Vol 32 No. 10s, 2025.

[41] A. Hore and D. Ziou, Image quality metrics: PSNR vs. SSIM. In 2010 20th International Conference on Pattern Recognition, pp. 2366-2369, 2010.

[42] H.T. Huynh,V.S. Lai, I. Soumaré, Stochastic simulation and applications in finance with matlab, John Wiley & Sonc, 2008.

[43] A. Ichikawa, Stability of Semilinear Stochastic Evolution Equations, J. Math. Anal. Appl.90, 12-44, 1982.

[44] F. Kanters, L. Florack, B. Platel, and B. ter Haar Romeny. Image reconstruction from multiscale critical points. In L. D. Griffin and M. Lillholm, editors, Scale-Space 2003, volume 2695 of Lecture Notes in Computer Science, pages 464ñ478. Springer, Berlin, 2003.

[45] S. Kataoka and M. Yasuda, Bayesian Image Denoising with Multiple Noisy Images, Volume 13, pages 267–280, 2019.

[46] S. Kichenassamy, The Perona-Malik paradox. SIAM Journal on Applied Mathematics, 57(5), pp.1328ñ1342, 1997.

[47] J.U. Kim, On a stochastic scalar conservation law, Indiana University Mathematics Journal, 52(1), p. 227-256, 2003.

[48] J. P. Khane, GILLES .P LEMERIE .R, Sèries de Fourier et ondelettes, Cassini, 1998.

[49] Jan J. Koendrink, The structure of images, Biol. Cybern, 363-370, 1984.

[50] P. Kornprobst, R. Deriche, and G. Aubert. Nonlinear operators in image restoration.In Proceedings of the International Conference on Computer Vision and Pattern Recognition, pp. 325-331, 1997.

[51] X. Li, T. Chen, Nonlinear diffusion with multiple edginess thresholds",Pattern Recognition, vol.27, no.8, pp.1029-1037, 1994.

[52] T. Lindeberg. Edge detection and ridge detection with automatic scale selection. International Journal of Computer Vision, 30(2):117-154, 1998.

[53] T. Lindeberg. Feature detection with automatic scale selection. International Journal of Computer Vision, 30(2):79-116, 1998.

[54] J.L. Lions, Quelques méthodes de résolutions des problèmes aux limites non linéaires, Dunod Gauthier Villars, Paris, 1969.

[55] P.A. Mayer, Probabilités et Potentiel, Herman, Paris, 1966.

[56] M. Métivier and J. Pellaumail, Stochastic Integration, Academic Press, New York, 1980.

[57] G.J. Minty, Monotone (non linear) operators in Hilbert spaces, Duke Math. J. 29,341-346, 1962.

[58] J.M. Morel and Rudin-Osher-Fatemi, Total variation denoising using split bregman, Image Processing On Line, Pascal Getreuer, 74-95, 2012.

[59] M. Nitzberg, T. Shiota, Nonlinear image filtering with edge and corner enhancement, IEEE Transactions on Pattern Analysis and Machine Intelligence, vol.14, no.8, pp. 826-833, 1992.

[60] F.Z. Nouri, Uniqueness and Existence Results for a partial Differential Equation in Image Inpainting, Commun. Optim. Theory (2020) Article ID7 1-17. https://doi.org/10.23952/cot. 2020.

[61] B. Øksendal, Stochastic differential equations, Universitext, Springer, (Sixth Edition), 2013.

[62] E. Pardoux, Stochastic Partial Differential Equations and Filtering of Diffusion Processes, Stochastic 3, 127-167, 1979.

[63] P. Perona and J. Malik, Scale-space and edge detection using anisotropic diffusion, IEEE Trans. Pattern Anal. Machine Intell., vol. 12, pp. 629-639, 1990.

[64] C. Prévot and M. RÖCKNER, A concise cours on stochastic partial differential equations, Springer, Lecture Notes in Mathematics, vol. 1905, 2007.

[65] J. Real, Stochastic Partial Differential Equations with Delays, Stochastics 8, 2, 81-102, 1982.

[66] L. I. Rudin, S. Osher and E. Fatemi, Nonlinear total variation based noise removal algorithms, Physica D: Nonlinear Phenomena, vol 60, p. 259-268, 1992.

[67] L. Schwartz, Radon measures on arbitrary topological spaces (à paraître), Tata institute of Fundamental Research Bombay, 1973.

[68] E.H. Soubari, Traitement d'images par transformer de Fourier optique, Departement Des Arts Graphiques, B.P. 6009-45060 Orléans Cédex, 1-40, 1979.

[69] N. Touzi, EDS retrogrades et EDP non lineaires, Conférence de la SMAI sur l'optimisation et la décision, Ecole Polytechnique, 2007.

[70] G. Vallet, Stochastic perturbation of nonlinear degenerate parabolic problems, Differential and Integral Equations, 21(11-12), 10551082, 2008.

[71] G. Vallet and P. Wittbold, On a Stochastic first-order hyparbolic equation in a Bounded Domain, Infinite Dimensional Analysis, Quantum Probability,12(4), p. 1-39, 2009.

[72] S.J. Walker, Fourier analysis and wavelet analysis, Notices of The AMS, 658-670, 1997.

[73] Z. Wang and A. C. Bovik, Mean squared error: love it or leave it?, IEEE Signal Processing Magazine, vol. 26, pp.98- 117, 2009.

[74] Y. Wang, G. Wei Wei, S. Yang, Partial differential equation tronsform variational formulation and Fourier Analysis, Int. J. Numer. Meth. Biomed. Engng. 1-25, 2011.

[75] J. Weickert, Anisotropic diffusion, in image processing vol. 1, pp. 59-60, 1998.

[76] J. Weickert, editors, Scale-Space and PDE Methods in Computer Vision, volume 3459 of Lecture Notes in Computer Science, pages 431-442. Springer, Berlin, 2005.

[77] R. Whitaker, Geometry limited diffusion, Thèse de doctorat, Department of Computer Science, University of North Carolina, 1993.

[78] A. Witkin, Scaleñspace Öltering, In: Proceedings of the International Joint Conference on ArtiÖcial Intelligence, New-York, pp. 1019-1021, 1983.

[79] D. Yong, Essential m-dissipativity of Kolmogorov Operators for the 2D-Stochastic shear thickening fluids, Volume 26, Issue 1, January 2, 2019.